

# Measurements of the reactions $^{12}\text{C}(\nu_\mu, \mu^-) ^{12}\text{N}_{g.s.}$ and

## $^{12}\text{C}(\nu_\mu, \mu^-) \text{X}$

C. Athanassopoulos<sup>12</sup>, L. B. Auerbach<sup>12</sup>, R. L. Burman<sup>7</sup>, D. O. Caldwell<sup>3</sup>,  
E. Church<sup>1</sup>, I. Cohen<sup>6</sup>, B. D. Dieterle<sup>10</sup>, J. B. Donahue<sup>7</sup>, A. M. Eisner<sup>4</sup>,  
A. Fazely<sup>11</sup>, F. J. Federspiel<sup>7</sup>, G. T. Garvey<sup>7</sup>, M. Gray<sup>3</sup>, R. M. Gunasingha<sup>1</sup>,  
R. Imlay<sup>8</sup>, K. Johnston<sup>9</sup>, H. J. Kim<sup>8</sup>, W. C. Louis<sup>7</sup>, R. Majkic<sup>12</sup>,  
K. McIlhany<sup>1</sup>, W. Metcalf<sup>8</sup>, G. B. Mills<sup>7</sup>, R. A. Reeder<sup>10</sup>, V. Sandberg<sup>7</sup>, D. Smith<sup>5</sup>,  
I. Stancu<sup>1</sup>, W. Strossman<sup>1</sup>, R. Tayloe<sup>7</sup>, G. J. VanDalen<sup>1</sup>, W. Vernon<sup>2,4</sup>, N. Wadia<sup>8</sup>,  
J. Waltz<sup>5</sup>, Y-X. Wang<sup>4</sup>, D. H. White<sup>7</sup>, D. Works<sup>12</sup>, Y. Xiao<sup>12</sup>, S. Yellin<sup>3</sup>

LSND Collaboration

<sup>1</sup>*University of California, Riverside, CA 92521*

<sup>2</sup>*University of California, San Diego, CA 92093*

<sup>3</sup>*University of California, Santa Barbara, CA 93106*

<sup>4</sup>*University of California Intercampus Institute for Research at Particle Accelerators, Stanford,  
CA 94309*

<sup>5</sup>*Embry Riddle Aeronautical University, Prescott, AZ 86301*

<sup>6</sup>*Linfield College, McMinnville, OR 97128*

<sup>7</sup>*Los Alamos National Laboratory, Los Alamos, NM 87545*

<sup>8</sup>*Louisiana State University, Baton Rouge, LA 70803*

<sup>9</sup>*Louisiana Tech University, Ruston, LA 71272*

<sup>10</sup>*University of New Mexico, Albuquerque, NM 87131*

<sup>11</sup>*Southern University, Baton Rouge, LA 70813*

<sup>12</sup>*Temple University, Philadelphia, PA 19122*

(July 7, 2018)

Abstract

Charged current scattering of  $\nu_\mu$  on  $^{12}\text{C}$  has been studied using a  $\pi^+$  decay-in-flight  $\nu_\mu$  beam at the Los Alamos Meson Physics Facility. A sample of  $56.8 \pm 9.6$  events satisfying criteria for the exclusive reaction  $^{12}\text{C}(\nu_\mu, \mu^-)^{12}\text{N}_{g.s.}$  was obtained using the large Liquid Scintillator Neutrino Detector (LSND). The observed flux-averaged cross section,  $(6.6 \pm 1.0 \pm 1.0) \times 10^{-41} \text{ cm}^2$ , agrees well with reliable theoretical expectations. A measurement was also obtained for the inclusive cross section to all accessible  $^{12}\text{N}$  states,  $^{12}\text{C}(\nu_\mu, \mu^-)\text{X}$ . This flux-averaged cross section is  $(11.2 \pm 0.3 \pm 1.8) \times 10^{-40} \text{ cm}^2$ , which is approximately half of that given by a recent Continuum Random Phase Approximation (CRPA) calculation.

14.60.Lm, 13.15.+g

## I. INTRODUCTION

Low energy neutrino-nucleus cross sections are of interest because of their application to nuclear structure studies and their importance as a base of information for low energy neutrino detectors. The cross sections contain contributions from both axial vector and polar vector nuclear currents and thus provide complementary information to that provided by electron-nucleus scattering, which is sensitive only to the nuclear polar vector currents.

Thus far, data exist only for neutrino scattering on carbon. Three experiments, E225 at LAMPF [1], the KARMEN experiment at the ISIS facility of the Rutherford Laboratory [2] and LSND [3], have measured both the exclusive reaction  $^{12}\text{C}(\nu_e, e^-)^{12}\text{N}_{\text{g.s.}}$  and the inclusive cross section  $^{12}\text{C}(\nu_e, e^-)^{12}\text{N}^*$  to all the accessible excited states of  $^{12}\text{N}$ . In these measurements the  $\nu_e$  flux arises from  $\mu^+$  decay at rest with  $E_\nu < 52.8$  MeV. As a result of the low neutrino energy, transitions occur almost entirely to a few low lying states of  $^{12}\text{N}$ , and 60 % of the total cross section is to the  $^{12}\text{N}$  ground state. The cross section for producing the  $^{12}\text{N}$  ground state can be predicted with an accuracy of  $\approx 2\%$  by using model independent form factors that can be reliably extracted from other measurements [4]. All three experimental measurements of the  $^{12}\text{C}(\nu_e, e^-)^{12}\text{N}_{\text{g.s.}}$  cross section agree well with the expected value. Calculation of the inclusive cross section to the excited states of  $^{12}\text{N}$  is model dependent and is a less certain procedure. The Fermi Gas Model (FGM) is not reliable in this instance because the low neutrino energy leads to momentum transfers ( $q < 100$  MeV/c) much smaller than the Fermi momentum (200 MeV/c) in carbon. Thus extensive modeling of the nuclear dynamics is necessary. A recent calculation [5] that includes the particle-hole correlations in a continuum random phase approximation (CRPA) agrees well with the  $^{12}\text{C}(\nu_e, e^-)^{12}\text{N}^*$  cross sections reported by the three experiments.

This paper expands on our earlier preliminary [6,7] results on the charged current  $\nu_\mu$  scattering from carbon at somewhat higher neutrino energies using the flux of  $\nu_\mu$  created by  $\pi^+$  decay in flight. The inclusive cross section is strongly energy and momentum transfer dependent. Thus the flux-averaged cross section for the reaction  $^{12}\text{C}(\nu_\mu, \mu^-)^{12}\text{N}^*$  is approx-

imately 200 times larger than the lower energy cross section for  $^{12}\text{C}(\nu_e, e^-)^{12}\text{N}^*$ . In this case, a CRPA calculation yields a cross section approximately twice the observed value [8]. This apparent discrepancy, between the good agreement of the CRPA calculation and measurements for the decay-at-rest result and the factor of two discrepancy between a similar calculation and this measurement for the decay-in-flight cross section, has generated considerable theoretical interest [8]. A large-basis shell-model calculation, however, obtains a result that is lower than the CRPA calculation for this reaction due to nuclear structure effects and may be consistent within errors with the observed value [9]. The only experiment previous to LSND had limited data and reported a cross section substantially above expectations and a muon energy spectrum much softer than expected [10]. These results are inconsistent with the LSND results [6,7].

This paper presents a detailed study of  $\nu_\mu$  carbon scattering based on data obtained in 1994 and 1995. Both the exclusive reaction  $^{12}\text{C}(\nu_\mu, \mu^-)^{12}\text{N}_{g.s.}$  and the inclusive reaction  $^{12}\text{C}(\nu_\mu, \mu^-)^{12}\text{N}$  are measured. The calculated  $\nu_\mu$  energy spectrum arising from  $\pi^+$  decay-in-flight is shown in Fig. 1. Also shown is the energy spectrum of the much smaller  $\bar{\nu}_\mu$  flux arising from  $\pi^-$  decay-in-flight. Neutrinos with energies between muon production threshold (123.1 MeV) and approximately 280 MeV contribute to the cross section; therefore much higher nuclear excitation energies are possible for  $\nu_\mu\text{C}$  scattering than for the  $\nu_e\text{C}$  measurement discussed above. The measurement of the exclusive reaction,  $^{12}\text{C}(\nu_\mu, \mu^-)^{12}\text{N}_{g.s.}$ , provides a valuable check on the overall analysis procedure because the cross section for this process can be reliably calculated in a mostly model independent fashion.

The analysis presented in this paper for events arising from decay-in-flight neutrinos is also important because of its relevance to the two searches for neutrino oscillations by LSND. Evidence has been presented [11] for  $\bar{\nu}_\mu \rightarrow \bar{\nu}_e$  oscillations using  $\bar{\nu}_\mu$  from  $\mu^+$  decay at rest. The backgrounds to this measurement from decay-in-flight neutrinos are expected to be small, but it is nevertheless important to measure these processes. LSND is also searching for  $\nu_\mu \rightarrow \nu_e$  oscillations using the decay-in-flight  $\nu_\mu$  beam by detecting electrons from the process  $^{12}\text{C}(\nu_e, e^-)^{12}\text{N}$ . For this search quantitative knowledge is required both of

the decay-in-flight neutrino beam and of neutrino-carbon cross sections.

## II. THE NEUTRINO SOURCE

The data reported here were obtained in 1994 and 1995 at the Los Alamos Meson Physics Facility (LAMPF) primarily using neutrinos produced at the A6 proton beam stop. As discussed below some neutrinos are also produced at upstream targets A1 and A2. The neutrino source is described in detail elsewhere [12]. This facility is now referred to as the Los Alamos Neutron Science Center (LANSCE). The beam stop consists of a 30-cm water target and a 50-cm pion decay region surrounded by steel shielding and followed by a copper beam dump. The high-intensity 800 MeV proton beam from the linear accelerator generates a large pion flux from the water target. The fluxes of  $\nu_\mu$  and  $\bar{\nu}_\mu$  used for the measurements reported here arise from the decay in flight (DIF) of  $\pi^+$  and  $\pi^-$ . For the LAMPF proton beam and beam stop configuration  $\pi^+$  production exceeds  $\pi^-$  production by a factor of approximately eight and even more for high energy pions. Approximately 3.4% of the  $\pi^+$  and 5% of the  $\pi^-$  decay in flight. The LAMPF proton beam typically had a current of 800  $\mu\text{A}$  and an energy of approximately 770 MeV at the A6 beam stop. The integrated beam current was 5904 C in 1994 and 7081 C in 1995. Upstream targets contributed 6% to the DIF neutrino flux. For the 1995 run, the water target was removed for 32% of the 7081 C of beam. For this portion of the run the DIF  $\nu_\mu$  flux was reduced approximately 50%. The  $\nu_\mu$  flux above muon production threshold (123.1 MeV) and averaged over the LSND detector was then  $6.75 \times 10^{11} \text{ cm}^{-2}$  for 1994 and  $6.50 \times 10^{11} \text{ cm}^{-2}$  for 1995. The  $\bar{\nu}_\mu$  flux above threshold (113.1 MeV) for the process  $\bar{\nu}_\mu + \text{p} \rightarrow \mu^+ + \text{n}$  was  $6.79 \times 10^{10} \text{ cm}^{-2}$  for 1994 and  $6.69 \times 10^{10} \text{ cm}^{-2}$  for 1995.

A detailed beam simulation program has been developed over the last decade to describe the LAMPF beam dump which has been used as the neutrino source for previous experiments E31 [13], E225 [1] and E645 [14]. A calibration experiment, E866 [15], measured the rate of stopped  $\mu^+$  from a low-intensity proton beam incident on an instrumented beam stop. The

rate of stopped  $\mu^+$  per incident proton was measured as a function of several variables and used to fine tune the beam dump simulation program [16]. This simulation program can then be used to calculate the flux for any particular beam dump configuration.

The calibration experiment determined the decay-at-rest flux to  $\pm 7\%$  uncertainty for the proton energies and beam stop configurations used at LAMPF. There are greater uncertainties in the DIF fluxes. Uncertainties in the energy spectra of the  $\pi^\pm$  which decay in flight lead to uncertainties in both the magnitudes and shapes of the  $\nu_\mu$  and  $\bar{\nu}_\mu$  energy spectra. The resulting uncertainty in the DIF flux for neutrinos above muon production threshold is estimated to produce an uncertainty in the measured cross section of 15%.

We have performed a significant test of the beam simulation by comparing data taken with two distinct beam dump configurations. As discussed above, the water target was removed for 32% of the 1995 data. Per Coulomb of proton beam the beam simulation program predicts a  $\nu_\mu$  flux above muon production threshold only 48% as large with the water target out as with the water target in. The predicted  $\nu_\mu$  energy spectrum is, however, harder with the water target out, so that the predicted rate for  $^{12}\text{C}(\nu_\mu, \mu^-)$  X events is  $61 \pm 4\%$  as large and the mean detected energy of these events is  $15 \pm 4\%$  larger. The systematic errors shown include a conservative estimate of the effect of the uncertainty in the energy dependence of the cross section. For comparison, the measured event rate with the water target out is  $57 \pm 5\%$  of the rate with the water target in. The mean event energy is  $13 \pm 4\%$  larger with the water target out. The good agreement with expectations for both the event rate and mean detected energy provides a valuable check of the beam simulation program.

### III. THE LSND DETECTOR

The detector is located 29.8 m downstream of the proton beam stop at an angle of  $12^\circ$  to the proton beam. Fig. 2 shows a side view of the setup. Approximately  $2000 \text{ g/cm}^2$  of shielding above the detector attenuates the hadronic component of cosmic rays to a low

level. Enclosing the detector, except on the bottom, is a highly efficient liquid scintillator veto shield which is essential to reduce contributions from the cosmic ray muon background to a low level. The detector is also well shielded from the beam stop so that beam-associated neutrons are attenuated to a negligible level. Ref. 12 provides a detailed description of the detector, veto and data acquisition system which we briefly review here.

The detector is a nearly cylindrical tank containing 167 tons of liquid scintillator and viewed by 1220 uniformly spaced 8" Hamamatsu photomultiplier tubes (PMTs) covering  $\sim 25\%$  of the surface inside the tank wall. The digitized time and pulse height of each of these PMTs (and of each of the 292 veto shield PMTs) are recorded when the deposited energy in the tank exceeds a threshold of approximately 4 MeV electron-equivalent energy, and there are fewer than 4 PMT hits in the veto shield. A veto, imposed for  $15.2 \mu\text{s}$  following the firing of  $> 5$  veto PMTs, substantially reduces ( $10^{-3}$ ) the large number of background events arising from the decay of cosmic ray muons that stop in the detector. Activity in the detector or veto shield during the  $51.2 \mu\text{s}$  preceding a primary trigger is also recorded provided there are  $> 17$  detector PMT hits or  $> 5$  veto PMT hits. This activity information is used in the analysis also to identify events arising from muon decay. In particular, in this analysis the activity information is used to identify low energy  $\mu^-$  from the reaction  $\nu_\mu + {}^{12}\text{C} \rightarrow \mu^- + X$ . For such events the  $e^-$  from the subsequent decay  $\mu^- \rightarrow e^- + \nu_\mu + \bar{\nu}_e$  provides the primary trigger. It should also be noted that the  $15.2 \mu\text{s}$  veto applies only to the primary trigger and not to the activities preceding a valid trigger.

Subsequent to a primary event trigger, data are recorded for 1 ms with a greatly reduced threshold of 21 PMTs (approximately 0.7 MeV electron energy equivalent). This low threshold is necessary to detect  $\gamma$ 's associated with neutron capture, as described below. The detector operates without reference to the beam spill, but the state of the beam is recorded with the event. Approximately 93% of the data is taken between beam spills. This allows an accurate measurement and subtraction of cosmic ray background surviving the event selection criteria.

The detector medium consists of mineral oil ( $\text{CH}_2$ ) in which is dissolved a small con-

centration (0.031 g/l) of b-PBD [17]. This mixture allows the detection of both Cerenkov light and approximately isotropic scintillation light and produces about 33 photoelectrons per MeV of electron energy deposited in the oil. The combination of the two sources of light provides direction information and makes particle identification (PID) possible for relativistic particles. Identification of neutrons is accomplished through the detection of the 2.2 MeV  $\gamma$  from neutron capture on free protons. Stopping  $\mu^-$  are captured on  $^{12}\text{C}$  8% of the time in the LSND detector. The  $\mu^\pm$  which decay are readily identified as muons by the presence of subsequent spatially correlated Michel electrons.

The veto shield encloses the detector on all sides except the bottom. The main veto shield [18] consists of a 15-cm layer of liquid scintillator. Additional counters were placed below the veto shield after the 1993 run to reduce cosmic ray background entering through the bottom support structure. These counters around the bottom support structure are referred to as bottom counters. A veto inefficiency  $< 10^{-5}$  is achieved with this veto system for incident charged particles.

#### IV. ANALYSIS TECHNIQUES

In the analysis presented in this paper we require a  $\mu^\pm$  followed by a delayed coincidence with a decay  $e^\pm$ . As a result of this coincidence requirement a clean beam excess sample of events can be obtained with relatively loose selection criteria. Furthermore, it is easy to verify that the events in this sample arise from muon decay since the muon lifetime and the decay electron energy spectrum are well known, and the response of the LSND detector to electrons from muon decay has been well determined from a large, clean sample of electrons from decays of stopping cosmic ray muons.

Each event is reconstructed using the hit time and pulse height of all hit PMTs in the detector. The present analysis relies on the reconstructed energy, position and particle ID parameter,  $\chi_{tot}$  [12]. The parameter  $\chi_{tot}$  is used to distinguish electrons from interactions of cosmic ray neutrons in the detector and will be explained below.

Fortunately, it is possible to measure the response of the detector to electrons and neutrons in the energy range of interest for this analysis. The response of the detector to electrons was determined from a large, essentially pure sample of electrons (and positrons) from the decay of stopped cosmic ray  $\mu^\pm$  in the detector. The known energy spectrum for electrons from muon decay was used to determine the absolute energy calibration including its small variation over the volume of the detector. The energy resolution was determined from the shape of the electron energy spectrum as shown in Fig. 3 and was found to be 6.6% at the 52.8 MeV endpoint. We also make use of a detailed Monte Carlo simulation, LSNDMC [19], which was written to simulate events in the detector using GEANT. The position resolution obtained from the LSNDMC simulation is approximately 30 cm for a 20 MeV electron.

For relativistic electrons in the LSND detector approximately 70% of the photoelectrons arise from direct or re-radiated Cerenkov light and only 30% from scintillator light. For muons, the threshold kinetic energy for Cerenkov radiation in the LSND detector is 39 MeV. For the sample of muons analyzed in this paper only about half are above Cerenkov threshold and none fully relativistic. As a result, the light output per MeV of energy loss for the muons is significantly less than that for relativistic electrons. There is no calibration sample available of low energy muons with known energies. Thus we rely on the Monte Carlo simulation LSNDMC for muons. We discuss the muon energy scale further in sections VI and VII when we compare observed and expected energy distributions.

There are no tracking devices in the LSND detector, and thus event positions must be determined solely from the PMT information. The reconstruction process determines an event position by minimizing a function  $\mathcal{X}_r$ , which is based on the time of each PMT hit corrected for the travel time of light from the assumed event position to the PMT [12]. This reconstruction procedure was found to systematically shift event positions away from the center of the detector and thus effectively reduces the fiducial volume [12], as discussed below. In the analysis presented in this paper a fiducial cut is imposed on the electron by requiring  $D > 35$  cm, where  $D$  is the distance between the reconstructed electron position

and the surface tangent to the faces of the PMTs.

The effect of the reconstruction bias on the fiducial acceptance was determined from the analysis of a sample of stopping muon events for which both the muon and the subsequent decay electron were detected. No fiducial cut was imposed on either the muon or the electron so that essentially all muons which stopped in the scintillator and decayed were included. For comparison a sample of simulated stopping muon events was generated using LSNDMC. The observed and generated distributions of the distance  $D$  were compared for electrons satisfying a minimum energy requirement. The observed distribution was found to be shifted outward relative to the generated distribution. Several independent analyses of this type yielded the acceptance factor of  $0.85 \pm 0.05$  for  $D > 35$  cm due to the reconstruction bias. There is independent support for this conclusion. A new reconstruction procedure has been developed which relies primarily on PMT pulse height rather than timing information and is not expected to have a significant bias. Comparison of vertex positions obtained with the new and the standard reconstruction procedures indicate an outward shift in good agreement with that obtained from the stopping muon analysis.

The particle identification procedure is designed to separate particles with velocities well above Cerenkov threshold from particles below Cerenkov threshold by making use of the four parameters defined in Ref. 12. Briefly,  $\mathcal{X}_r$  and  $\mathcal{X}_a$  are the quantities minimized for the determination of the event position and direction,  $\mathcal{X}_t$  is the fraction of PMT hits that occur more than 12 ns after the fitted event time and  $\chi_{tot}$  is proportional to the product of  $\mathcal{X}_r$ ,  $\mathcal{X}_a$  and  $\mathcal{X}_t$ . For the present analysis we use only  $\chi_{tot}$  and impose a requirement only on the electron candidate, not on the preceding muon candidate. Figure 4 shows the  $\chi_{tot}$  distributions for electrons from stopping  $\mu$  decay and for cosmic ray neutrons with electron-equivalent energies in the  $16 < E_e < 60$  MeV range. For a neutron  $E_e$  is the equivalent electron energy corresponding to the observed total charge. In the present analysis a relatively loose  $\chi_{tot}$  requirement reduces the neutron background to a negligible level.

The presence of a neutron can be established from the neutron capture reaction  $n + p \rightarrow d + \gamma$ . The mean capture time in the LSND detector is expected to be 186  $\mu$ s,

essentially independent of the initial neutron energy. Three variables are used to identify a capture  $\gamma$  correlated with a neutron in the primary event: the number of PMT hits for the  $\gamma$ , the distance of the  $\gamma$  from the primary event and the time of the  $\gamma$  from the primary event. Fig. 5 shows the distributions of these variables for correlated  $\gamma$ 's and for uncorrelated (accidental)  $\gamma$ 's. A likelihood technique, discussed in Ref. 11, has been developed to separate the correlated component due to neutrons from the uncorrelated component. An approximate likelihood ratio  $R \equiv \mathcal{L}_{cor}/\mathcal{L}_{uncor}$  is calculated for each event from the three measured variables. If there is no  $\gamma$  within 1 ms and 2.5 m from the primary event then  $R = 0$  for the event. The expected distributions of  $R$  are shown in Fig. 6 for a correlated sample (every event has one neutron) and for an uncorrelated sample (no event has a neutron). The correlated  $R$  distribution was found to be almost independent of event position within the fiducial volume [11]. The accidental gamma rate is higher near the bottom front corner of the detector than elsewhere, but the shape of the uncorrelated  $R$  distribution has little position dependence. Also shown in Fig. 6 is the measured  $R$  distribution [3] for a clean sample of over 500 events from the reactions  $^{12}\text{C}(\nu_e, e^-)^{12}\text{N}_{g.s.}$ . Such events have no associated neutrons and thus this sample provides a useful check of the uncorrelated  $R$  distribution. The agreement with the distribution for uncorrelated  $\gamma$ 's is excellent. In the present paper we use the  $\gamma$  analysis to determine the fraction of the events in the DIF sample that are accompanied by neutrons. The measured  $R$  distribution is fit to a mixture of the correlated and uncorrelated distributions shown in Fig. 6, and the fraction of events with neutrons is obtained.

Beam-off data taken between beam spills play a crucial role in the analysis of this experiment. Most event selection criteria are designed to reduce the background due to cosmic rays while retaining high acceptance for the neutrino process of interest. The cosmic ray background which remains after all selection criteria have been applied is well measured with the beam-off data and subtracted using the duty ratio, the ratio of beam-on time to beam-off time. This ratio was 0.080 for 1994 and 0.060 for 1995. The smaller duty ratio in 1995 arose from changes in LAMPF beam operations, especially a reduction in the number

of proton beam spills per second at the A6 beam dump.

## V. EVENT SELECTION

The analysis is designed to select the  $\mu^-$  from the reaction  $\nu_\mu + {}^{12}\text{C} \rightarrow \mu^- + \text{X}$  and the subsequent electron from the decay  $\mu^- \rightarrow e^- + \bar{\nu}_e + \nu_\mu$ . In the LSND detector medium 92% of the stopped  $\mu^-$  decay and 8% are captured. The  $\mu^-$  and other particles arising from the charge-changing neutrino interaction produce light that causes an average of 250 PMTs to fire. The detector signal,  $Q_\mu$ , measured in photoelectrons arises mostly from the  $\mu^-$  but includes contributions from other particles produced in the reaction such as protons and gammas.

Table I shows the selection criteria and corresponding efficiencies for the muon and electron for events in which there are more than 100 PMT hits at the time of the  $\mu^-$ . Slightly tighter criteria, discussed below, are used for the  $\sim 10\%$  of the events with fewer than 100 PMT hits. These two samples are referred to as “high energy  $\mu$ ” and “low energy  $\mu$ ”, respectively. For events in the decay-in-flight sample the event position is best determined from the reconstructed electron position rather than the reconstructed muon position, especially for events with low energy muons. Therefore, the fiducial selection is imposed primarily on the electron. The reconstructed electron position is required to be a distance  $D > 35$  cm from the surface tangent to the faces of the PMTs. There are  $3.65 \times 10^{30}$   ${}^{12}\text{C}$  nuclei within this fiducial volume. The muon is required to reconstruct only inside the region  $D > 0$  cm. A lower limit on the electron energy of 16.0 MeV eliminates the large background from  ${}^{12}\text{B}$  beta decay created by the capture of cosmic ray  $\mu^-$  on  ${}^{12}\text{C}$ . Fig. 7 shows the observed electron energy distribution compared with that obtained from a large clean sample of Michel electrons from decays of stopping cosmic ray muons. The distribution of the time,  $\Delta t_{\mu e}$ , between the muon and electron candidates, shown in Fig. 8, agrees well with the  $2.03 \mu\text{s}$   $\mu^-$  lifetime in mineral oil. The best fit, also shown, corresponds to a lifetime  $1.98 \pm 0.06 \mu\text{s}$ . The requirement  $\Delta t_{\mu e} \geq 0.7 \mu\text{s}$  is imposed to insure that the  $\mu$  and e are clearly separated

in the trigger and in the readout of the data. The excellent agreement with expectations in Fig. 7 and 8 clearly show that the events arise from muon decay. There is an 8% loss of events due to  $\mu^-$  capture in the detector medium. Fig. 9 shows the spatial separation,  $\Delta r$ , between the reconstructed muon and electron positions. A loose requirement,  $\Delta r < 1.5$  m, is imposed to minimize the background from accidental  $\mu, e$  correlations while retaining high acceptance.

Many of the selection criteria are designed to reduce the cosmic ray background, especially that arising from the decay of cosmic ray muons which stop in the detector. Events are required to have fewer than 4 PMT hits in the veto at both the muon time and the electron time. The detector PMT faces are 25 cm inside the tank and thus stopping cosmic ray muons must traverse at least 60 cm of scintillator to reach the fiducial volume. As a result these muons typically produce a large detector signal. The requirement  $Q_\mu < 2000$  pe, where  $Q_\mu$  is the detector signal at the muon time measured in photoelectrons, eliminates most such background events with almost no loss of acceptance for muons arising from neutrino interactions.

Frequently, in addition to the candidate muon which satisfies the criteria in Table I, there are one or more other activities prior to the electron. If an activity is due to a stopping muon, that muon could be the parent of the observed electron. Therefore an event is rejected if, in the 35  $\mu s$  interval prior to the electron, there is an activity with  $Q > 3000$  pe or an activity with  $> 4$  PMT hits in the veto and  $> 100$  PMT hits in the detector. This results in a 7% loss of efficiency for neutrino events. The efficiency for the past activity criteria shown in Table I also includes the effect of the veto that is applied for 15.2  $\mu s$  following any event with  $> 5$  PMT hits in the veto shield.

The acceptances for the past activity and in-time veto cuts are obtained by applying these cuts to a large sample of events triggered with the laser used for detector calibration. These laser events are spread uniformly through the run and thus average over the small variation in run conditions.

Only a loose particle ID requirement,  $\mathcal{X}_{tot} < 1.0$ , was imposed on the electron and none

on the muon. A sample of Michel electrons (electrons from the decay of stopped  $\mu^\pm$ ) was analyzed to obtain the acceptance of electrons for the  $\chi_{tot}$  particle identification cut as shown in Fig. 4.

For events in which fewer than 100 PMT hits occur at the muon time (low energy  $\mu$  events) tighter selection criteria are needed to keep the beam-off background small. These tighter criteria are: (1) electron particle ID ( $\mathcal{X}_{tot} < 0.8$  instead of 1.0), (2) muon decay time ( $\Delta t_{\mu e} < 6.6\mu s$  instead of  $9.0\mu s$ ) and (3) a tighter past activity cut. As a result, the efficiency for this inclusive “low energy  $\mu$ ” sample is only  $67 \pm 1\%$  of the “high energy  $\mu$ ” sample efficiency. This includes the small loss of acceptance for muons below the 18 PMT detection threshold.

The Monte Carlo simulation LSNDMC was used to obtain the PMT hits distributions expected from the various processes that contribute to the inclusive sample and to the exclusive sample with an identified beta decay. Fig. 10 compares the observed and expected distributions of PMT hits for inclusive events. There is excellent agreement, and thus we expect that the simulation provides a reliable estimate of the fraction of “low energy  $\mu$ ” events below 18 PMT hits (roughly 4 MeV). For the inclusive sample (exclusive sample) we find that only 6% (18%) of the “low energy  $\mu$ ” events have fewer than 18 PMT hits. The overall efficiency for the inclusive (exclusive) “low energy  $\mu$ ” sample is 67% (61%) of the efficiency for the “high energy  $\mu$ ” sample.

For analysis of the exclusive process  $^{12}\text{C}(\nu_\mu, \mu^-)^{12}\text{N}_{g.s.}$  we also require detection of the  $e^+$  from the beta decay of  $^{12}\text{N}_{g.s.}$ . Therefore, for these events three particles are detected: the muon, the decay electron and the positron from the beta decay of  $^{12}\text{N}_{g.s.}$ . Table II gives the selection criteria and efficiencies for the  $^{12}\text{N}$  beta decay positron. These are the same criteria [3] used previously in an analysis of a sample of over 500 events from the analogous process  $^{12}\text{C}(\nu_e, e^-)^{12}\text{N}_{g.s.}$ . The beta decay has a mean lifetime of 15.9 ms and maximum positron kinetic energy of 16.3 MeV. Fig. 11 shows the observed beta decay time distribution compared with the expected 15.9 ms lifetime. Fig. 12 shows the distance between the reconstructed electron and positron positions for the beam-excess sample. For

comparison, the distribution observed for the  $^{12}\text{C}(\nu_e, e^-)^{12}\text{N}_{g.s.}$  sample is shown by the solid line. A cut was applied at 100 cm resulting in an acceptance of  $(96 \pm 2)\%$ . The positron is required to be spatially correlated with the electron rather than the muon because the position of the electron in general is better determined. Following a muon produced by a neutrino interaction, an uncorrelated particle, such as the positron from  $^{12}\text{B}$  beta decay, will occasionally satisfy all the positron criteria including the requirements of time (45 ms) and spatial (1 m) correlation with the electron. The probability of such an accidental coincidence can be precisely measured from the Michel electron sample. The background from this source is also shown in Figs. 11 and 12. The efficiency of 81.5% caused by the 15.2  $\mu\text{s}$  veto and the trigger dead time of 3% are the same as for the electron. Positrons with 4 or more in-time veto hits or any bottom veto coincidence are rejected. The Monte Carlo was used to generate expected distributions for the positron energy. There was a trigger requirement of 100 PMT hits for 1994 and 75 PMT hits for 1995. The positron was required to have an energy less than 18 MeV. Fig. 13 compares the observed and expected positron energy distributions. Fig. 14 compares the observed and expected energy distributions of the electron from the muon decay, and Fig. 15 compares the observed and expected distributions of muon decay time.

Table III shows the numbers of beam-on, beam-off and beam-excess events satisfying the “high energy  $\mu$ ” and “low energy  $\mu$ ” selection criteria. The “low energy  $\mu$ ” events are given a weight to compensate for the lower efficiency for this sample. This allows the relatively small “low energy  $\mu$ ” sample to be combined with the “high energy  $\mu$ ” sample for the rest of the analysis. The sample of inclusive  $\mu$ -e events is used for the analysis of the reaction  $\nu_\mu + ^{12}\text{C} \rightarrow \mu^- + \text{X}$ , while the exclusive sample of events with an identified beta decay is used for analysis of the reaction  $\nu_\mu + ^{12}\text{C} \rightarrow \mu^- + ^{12}\text{N}_{g.s.}$ .

## VI. THE TRANSITION TO THE $^{12}\text{N}$ GROUND STATE

The reaction  $\nu_\mu + ^{12}\text{C} \rightarrow ^{12}\text{N}_{g.s.} + \mu^-$  is identified by the detection of the  $\mu^-$ , the  $e^-$  from the decay  $\mu^- \rightarrow e^- + \nu_\mu + \bar{\nu}_e$  and the positron from the  $\beta$  decay of the  $^{12}\text{N}_{g.s.}$ . This three-fold delayed coincidence requirement provides a distinctive event signature. Excited states of  $^{12}\text{N}$  decay by prompt proton emission and thus do not feed down to the  $^{12}\text{N}$  ground state or contribute to the delayed coincidence rate. The form factors required to calculate the cross section are well known from a variety of previous measurements [4]. This cross section and the known  $\nu_\mu$  flux are used to obtain the expected muon kinetic energy spectrum which is compared with the data in Fig. 16.

As stated in Section IV the energy calibration for muons (the conversion from photoelectrons to MeV) is obtained from the Monte Carlo simulation LSNDMC. For this ground state reaction, the expected muon energy distribution should be very reliable. Thus the good agreement seen in Fig. 16 provides confirmation for the muon energy calibration within the limited statistics.

There are two sources of background. The largest arises from the accidental coincidence of a positron candidate with an event from the inclusive sample of neutrino-induced muons. The probability of an uncorrelated particle satisfying all the positron criteria, including the requirements of time (45 ms) and spatial correlation (1 m) with the electron, can be precisely measured from a large Michel electron sample. The probability was 0.57% for 1994 and 0.84% for 1995. The probability is higher in 1995 because a lower PMT threshold was required that year for the positron. The second background arises from the process  $^{12}\text{C}(\bar{\nu}_\mu, \mu^+)^{12}\text{B}_{g.s.}$ , where we detect the  $e^-$  from the beta decay of the  $^{12}\text{B}$  ground state [20]. This background is small primarily because the flux of high energy  $\bar{\nu}_\mu$  is approximately a factor of ten lower than the corresponding  $\nu_\mu$  flux and because the  $^{12}\text{B}_{g.s.}$  lifetime is longer than the  $^{12}\text{N}_{g.s.}$  lifetime.

Table IV shows the number of beam excess events, the number of background events, the “high energy  $\mu$ ” efficiency, the neutrino flux for  $E_\nu > 123.1$  MeV and the cross section

averaged over the flux. The predicted flux-averaged cross section shown in Table IV was calculated for the flux shape for the 1994 LSND beam dump configuration and not for the average of the two years of data. Therefore, the measured flux-averaged cross section in Table IV has been adjusted slightly so that it also corresponds to the 1994 configuration. The flux-averaged cross section is

$$\langle \sigma \rangle = (6.6 \pm 1.0 \pm 1.0) \times 10^{-41} \text{cm}^2,$$

where the first error is statistical and the second systematic. The two dominant sources of systematic error are the neutrino flux (15%) discussed in section II and the effective fiducial volume (6%) discussed in section IV. The measured cross section is in very good agreement with the predicted cross section of  $6.4 \times 10^{-41} \text{cm}^2$  [20]. There is very little uncertainty in this predicted cross section for the exclusive process, as it is determined from measured form factors in related electro-weak processes. If we assume that it is correct, we can use our measurement to determine the  $\nu_\mu$  flux instead of the cross section. This yields a value for the  $\nu_\mu$  flux above the muon production threshold that is  $(105 \pm 16)\%$  of the value calculated using the beam Monte Carlo, if we assume the shape of the  $\nu_\mu$  flux is correctly given by the Monte Carlo. This excellent agreement provides a valuable confirmation of our understanding of the flux from the neutrino source.

For this reaction to the  $^{12}\text{N}$  ground state it is also straightforward to measure the energy dependence of the cross section. The recoil energy of the nucleus is small and to a very good approximation,  $E_\nu = m_\mu c^2 + T_\mu + 17.7 \text{ MeV}$ , where  $m_\mu$  is the muon mass,  $T_\mu$  the muon kinetic energy and 17.7 MeV arises from the Q value of the reaction and the nuclear recoil. Fig. 17 compares the measured cross section as a function of  $E_\nu$  with four theoretical calculations obtained from Ref. 20. The agreement is excellent within the limited statistics.

## VII. THE INCLUSIVE REACTION

Most of the inclusive beam-excess events arise from the reaction  $^{12}\text{C}(\nu_\mu, \mu^-)X$ , but approximately 10% are due to other sources. Table V shows the number of beam-excess

events, the calculated backgrounds, the “high energy  $\mu$ ” efficiency,  $\nu_\mu$  flux and the flux-averaged cross section for this process. The backgrounds arising from the  $\bar{\nu}_\mu$  component of the decay-in-flight beam are small, primarily because the high energy  $\bar{\nu}_\mu$  flux is approximately a factor of ten lower than the corresponding  $\nu_\mu$  flux. The largest background arises from the process  $\bar{\nu}_\mu + p \rightarrow \mu^+ + n$ . The cross section is well known and the uncertainty in this process is mainly due to the 15% uncertainty in the  $\bar{\nu}_\mu$  flux. A much smaller but less well understood background arises from the process  $^{12}\text{C}(\bar{\nu}_\mu, \mu^+)X$ . Plausibly, as observed for the process  $^{12}\text{C}(\nu_\mu, \mu^-)X$ , the cross section might be expected to be approximately 60% of that given by a recent CRPA calculation [8]. We use this reduced cross section in calculating this background but assign a large error to reflect the uncertainty in the cross section. An even smaller background arises from the 1.1%  $^{13}\text{C}$  component of the scintillator. For the process  $^{13}\text{C}(\nu_\mu, \mu^-)X$  we use a Fermi Gas Model calculation and assign a 50% uncertainty.

The measured flux-averaged cross section for the inclusive reaction  $^{12}\text{C}(\nu_\mu, \mu^-)X$  is

$$\langle \sigma \rangle = (11.2 \pm 0.3 \pm 1.8) \times 10^{-40} \text{cm}^2,$$

where the first error is statistical and the second systematic. The mean energy of the neutrino flux above threshold is 156 MeV. The systematic error is due almost entirely to the uncertainty in the  $\nu_\mu$  flux. The inputs to the neutrino beam Monte Carlo program were varied within the estimated uncertainties. The resulting variation in both the magnitude and the shape of the  $\nu_\mu$  flux above muon production threshold results in a 15% uncertainty in the inclusive cross section. As discussed in section VI, the flux-averaged cross section has been adjusted so that it corresponds to the flux shape from the 1994 beam dump configuration and not the average of the two years of data. This was done to permit direct comparison with the CRPA calculation of Ref. [8] which was performed for the 1994  $\nu_\mu$  flux. Ref. [8] predicts a flux-averaged cross section of  $20.5 \times 10^{-40} \text{cm}^2$  which is significantly higher than that measured. The measured cross section reported in this paper is  $2\sigma$  higher than that originally reported by LSND [6]. A substantial part of the increase arises from a better understanding of the loss of acceptance due to the spatial reconstruction program shifting

events outward as discussed in section IV.

The spatial distribution of the beam-excess electrons is shown in Fig. 18. There is a clear enhancement of events at high x and high y due to the variation of the  $\nu_\mu$  flux over the detector. The good agreement with expectation shows that this spatial distribution is well modeled by the beam simulation program.

For the reaction  $^{12}\text{C}(\nu_\mu, \mu^-)\text{X}$ , the detector signal,  $Q_\mu$ , measured in photoelectrons, arises mostly from the  $\mu^-$  but includes contributions from other particles in the reaction such as protons and gammas. The muon kinetic energy distribution can be obtained from the  $Q_\mu$  distribution by subtracting the contributions of these other particles. The average contributions from proton and  $\gamma$ 's are estimated to be 9 MeV and 2.9 MeV, respectively [8]. We used the calculation of Ref. 8 to determine proton and  $\gamma$  energy distributions and LSNDMC to determine the number of photoelectrons produced. Protons produce less scintillation light than electrons due to saturation effects. The uncertainty in the saturation effect is the primary source of uncertainty in the muon and proton energy determination. The average contribution to  $Q_\mu$  from particles other than the muon is approximately 20% using the CRPA calculation. The information available in Ref. 8 permits us to subtract the protons and  $\gamma$  contributions with a procedure that is only correct on average. The resulting  $E_\mu$  distribution should, however, be fairly reliable since the mean correction to  $Q_\mu$  is only 20%. Fig. 19 compares the observed distribution of  $E_\mu$  with the shape expected from a recent CRPA calculation which has been normalized to the data. There is fair agreement. However, given the uncertainties in the shape of the  $\nu_\mu$  energy spectrum, in the modeling of the energy from nuclear breakup and in the muon and proton energy calibration, we do not try to extract any information on the energy dependence of the cross section for the reaction  $^{12}\text{C}(\nu_\mu, \mu^-)\text{X}$ .

Further information on the inclusive sample can be obtained by measuring the fraction of the events with an associated neutron. The presence of a neutron is established by detection of the gamma ray from the neutron's capture on a proton in the detector via the reaction  $n + p \rightarrow d + \gamma$ . The  $\gamma$ 's are detected using the procedure discussed in section IV.

The distribution of the likelihood ratio  $R$  for correlated  $\gamma$ 's from neutron capture is very different from that for uncorrelated (accidental)  $\gamma$ 's. The measured  $R$  distribution for the inclusive sample, shown in Fig. 20, was fit to a mixture of the two possible gamma sources to determine the fraction of events with associated neutrons. The best fit, also shown in the figure, corresponds to a fraction of events with a neutron of  $(10.8 \pm 1.8)\%$ , where the error includes systematic uncertainties.

The two largest backgrounds shown in Table V arise from the  $\bar{\nu}_\mu$  component of the beam, and almost all of these events should have an associated neutron. In contrast, most of the events arising from  $\nu_\mu$  interactions will not have an associated neutron. A CRPA calculation predicts that 79% of the events from the reaction  $^{12}\text{C}(\bar{\nu}_\mu, \mu^+)\text{X}$  will have an associated neutron compared to only 5.9% for the reaction  $^{12}\text{C}(\nu_\mu, \mu^-)\text{X}$  [8].

Table VI shows the measured component with an associated neutron for the beam excess sample, the calculated backgrounds from  $\bar{\nu}_\mu$  interactions and the resulting numbers for the  $\nu_\mu$  carbon sample. The percentage of events with neutrons for the  $\nu_\mu$  carbon sample,  $(1.9 \pm 2.6)\%$ , is lower than but consistent with the CRPA prediction of 5.9%. The observed number of events with neutrons also rules out a  $\bar{\nu}_\mu$  flux much bigger than that calculated by the beam Monte Carlo.

## VIII. CONCLUSIONS

The exclusive process  $^{12}\text{C}(\nu_\mu, \mu^-)^{12}\text{N}_{g.s.}$  has been measured with a clean sample of  $56.8 \pm 9.6$  events for which the  $\mu^-$ , the decay  $e^-$  and the  $e^+$  from the beta decay of the  $^{12}\text{N}_{g.s.}$  are detected. For this process the cross section calculations are very reliable. The flux-averaged cross section is measured to be  $(6.6 \pm 1.0 \pm 1.0) \times 10^{-41} \text{ cm}^2$  in good agreement with theoretical expectations. From comparison of this cross section with the cross section for the inclusive process  $^{12}\text{C}(\nu_\mu, \mu^-)\text{X}$  we obtain a flux-averaged branching ratio of  $(5.9 \pm 0.9 \pm 0.6)\%$

The inclusive process  $^{12}\text{C}(\nu_\mu, \mu^-)\text{X}$  has also been measured. There are model dependent uncertainties in the calculated cross section for this process that are not present for the

$^{12}\text{N}_{g.s.}$  cross section. The flux-averaged cross section is found to be  $(11.2 \pm 0.3 \pm 1.8) \times 10^{-40}$   $\text{cm}^2$ , about 55% of a recent CRPA calculation [8]. The mean energy of the neutrino flux above threshold is 156 MeV. The measured distribution of the muon energy (including contributions from other particles such as protons and gammas) agrees within errors with the CRPA calculation [8]. The fraction of events with associated neutrons was measured to be  $(1.9 \pm 2.6)\%$ . This is lower than, but consistent with, the CRPA calculation of 5.9%.

As discussed above, there has been considerable interest in the fact that our observed cross section for the inclusive reaction  $\nu_\mu + ^{12}\text{C} \rightarrow \mu^- + \text{X}$  is only  $0.55 \pm 0.09$  of the result obtained in a sophisticated CRPA calculation [8] for the same process. Such CRPA calculations have to be tuned to fit the cross sections to final bound states, but without further adjustments to continuum final states. The CRPA calculation also reproduces the inclusive cross section (to well within the 17% experimental error) for the process  $\nu_e + ^{12}\text{C} \rightarrow e^- + ^{12}\text{N}^*$ , where the  $\nu_e$  arise from  $\mu^+$  decay at rest ( $E_\nu < 52.8$  MeV) [3]. The situation has been discussed in some detail in Ref. 8 but we wish to make some further observations. First, the agreement between the CRPA calculation of  $\nu_\mu + ^{12}\text{C} \rightarrow \mu^- + \text{X}$  and the newer data presented here is better,  $55 \pm 9\%$  rather than  $43 \pm 9\%$ . A possible reason that the calculation agrees with  $\mu^-$  capture and the low energy  $\nu_e$  inclusive scattering but fails in the case of the higher energy  $\nu_\mu$  is that both the muon capture and the  $\nu_e$  processes involve only low partial waves  $l = 0, 1$ . The momentum transfers for the  $\nu_\mu$  reaction (100-400 MeV/c) are much larger than for the lower energy  $\nu_e$  and muon capture processes ( $< 100$  MeV/c). Thus the former reaction can involve partial waves through  $l = 3, 4$ , values not probed by the lower energy processes. It is necessary to point out that no conclusion can be drawn from our results on the ratio of  $\nu_\mu$  to  $\nu_e$  cross sections as the measurements involved very different neutrino energies and momentum transfers. However, it appears that factor of two discrepancies may exist between sophisticated calculations and measured inclusive yields. This makes it difficult to have confidence that for the lower energy atmospheric neutrino data [21,22], which is only slightly above the LSND energy region, the observed lepton rates can be reliably converted into absolute neutrino fluxes.

*Acknowledgments* The authors gratefully acknowledge the support of Peter Barnes, Cyrus Hoffman, and John McClelland. This work was conducted under the auspices of the US Department of Energy, supported in part by funds provided by the University of California for the conduct of discretionary research by Los Alamos National Laboratory. This work is also supported by the National Science Foundation. We are particularly grateful for the extra effort that was made by these organizations to provide funds for running the accelerator at the end of the data taking period in 1995.

## TABLES

TABLE I. The muon and electron selection criteria and corresponding efficiencies for events with more than 100 PMT hits at the muon time.

Quantity	Criteria	Efficiency
Fiducial Volume e	$D > 35.0$ cm	$0.850 \pm 0.050$
Fiducial Volume $\mu$	$D > 0$	$0.950 \pm 0.005$
Electron Energy	$16 < E_e < 60$ MeV	$0.890 \pm 0.005$
Muon Charge	$Q < 2000$ pe	$0.990 \pm 0.010$
Electron Particle ID	$\chi_{tot} < 1.0$	$0.976 \pm 0.005$
Intime Veto $\mu, e$	$< 4$ PMTs	$0.984 \pm 0.007$
Past Activity	$\Delta t_p > 35$ $\mu s$	$0.750 \pm 0.010$
$\mu$ Decay Time	$0.7 < t < 9.0$ $\mu s$	$0.687 \pm 0.005$
Not $\mu^-$ Capture		$0.922 \pm 0.005$
Spatial Correlation	$\Delta r < 1.5$ m	$0.993 \pm 0.002$
DAQ Dead Time		$0.970 \pm 0.010$
Total		$0.313 \pm 0.020$

TABLE II. Beta decay  $e^+$  selection criteria and corresponding efficiencies for the reaction  $^{12}\text{C}(\nu_\mu, \mu^-)^{12}\text{N}_{g.s.}$ .

Quantity	Criteria	Efficiency
$\beta$ Decay Time	$52 \mu\text{s} < t < 45 \text{ ms}$	$0.938 \pm 0.002$
Spatial Correlation	$\Delta r < 1 \text{ m}$	$0.964 \pm 0.020$
PMT Threshold	$>100$ for 1994, $>75$ for 1995	$0.823 \pm 0.015$
Fiducial Volume	$D > 0 \text{ cm}$	$0.972 \pm 0.010$
Trigger Veto	$>15.2 \mu\text{s}$	$0.815 \pm 0.005$
Intime Veto	$<4$ PMTs	$0.992 \pm 0.001$
DAQ Dead Time		$0.970 \pm 0.010$
Total		$0.568 \pm 0.017$

TABLE III. Inclusive events and events with an identified beta decay. Events are classified as “high energy  $\mu$ ” (“low energy  $\mu$ ”) if there are more than (less than) 100 PMT hits at the time of the muon. The “low energy  $\mu$ ” events are given a weight to compensate for the reduced efficiency for the “low energy  $\mu$ ” sample.

	Inclusive Events		Events with beta decay	
	“high energy $\mu$ ” $>100$ PMTs	“low energy $\mu$ ” $<100$ PMTs	“high energy $\mu$ ” $>100$ PMTs	“low energy $\mu$ ” $<100$ PMTs
Beam-on	1755	176	47	16
Beam-off $\times$ Duty Ratio	39	23	1	0
Beam-excess $\times$ Weight	1716	$153 \times 1.48$	46	$16 \times 1.65$
Total beam-excess	$1942 \pm 46$		$72.4 \pm 9.5$	

TABLE IV. Beam-excess events, background, efficiency, neutrino flux and flux-averaged cross section for the exclusive reaction  $^{12}\text{C}(\nu_\mu, \mu^-)^{12}\text{N}_{g.s.}$

Corrected beam excess events	$72.4 \pm 9.5$
$\bar{\nu}_\mu + ^{12}\text{C} \rightarrow \mu^+ + ^{12}\text{B}_{g.s.}$ background	$2.0 \pm 0.4$
accidental $e^+$ background	$13.6 \pm 1.4$
$\nu_\mu + ^{12}\text{C} \rightarrow \mu^- + ^{12}\text{N}_{g.s.}$	$56.8 \pm 9.6$
“high energy $\mu$ ” efficiency	$0.178 \pm 0.013$
$\nu_\mu$ flux ( $E_\nu > 123.1$ MeV)	$1.33 \times 10^{12} \text{ cm}^{-2}$
$\langle \sigma \rangle$ measured	$(6.6 \pm 1.0 \pm 1.0) \times 10^{-41} \text{ cm}^2$
$\langle \sigma \rangle$ theory	$6.4 \times 10^{-41} \text{ cm}^2$

TABLE V. Beam excess events, background, efficiency, neutrino flux and flux averaged cross section for the inclusive reaction  $^{12}\text{C}(\nu_\mu, \mu)\text{X}$ .

Corrected Beam-excess events	$1942 \pm 46$
$\bar{\nu}_\mu + \text{p} \rightarrow \mu^+ + \text{n}$ background	$140 \pm 22$
$\bar{\nu}_\mu + ^{12}\text{C} \rightarrow \mu^+ + \text{X}$ background	$46 \pm 23$
$\nu_\mu + ^{13}\text{C} \rightarrow \mu^- + \text{X}$ background	$18 \pm 9$
$\nu_\mu + ^{12}\text{C} \rightarrow \mu^- + \text{X}$	$1738 \pm 56$
“high energy $\mu$ ” efficiency	$0.313 \pm 0.020$
$\nu_\mu$ Flux ( $E_\nu > 123.1$ MeV)	$1.33 \times 10^{12} \text{ cm}^2$
$\langle \sigma \rangle$ measured	$(11.2 \pm 0.3 \pm 1.8) 10^{-40} \text{ cm}^2$
$\langle \sigma \rangle$ CRPA model	$20.5 \times 10^{-40} \text{ cm}^2$

TABLE VI. The expected and observed numbers of events with associated neutrons and the calculated background from  $\bar{\nu}_\mu$  reactions.

Source	Events from Table V	Fraction with neutron	Events with neutron
Beam Excess	1942	(10.8±1.8)%	210 ± 35
$\bar{\nu}_\mu$ p $\rightarrow$ $\mu^+$ n	140	100%	140±22
$\bar{\nu}_\mu$ C $\rightarrow$ $\mu^+$ nX	46	79%	36±18
$\nu_\mu$ C $\rightarrow$ $\mu^-$ X	1756	1.9±2.6%	34±45

FIGURES

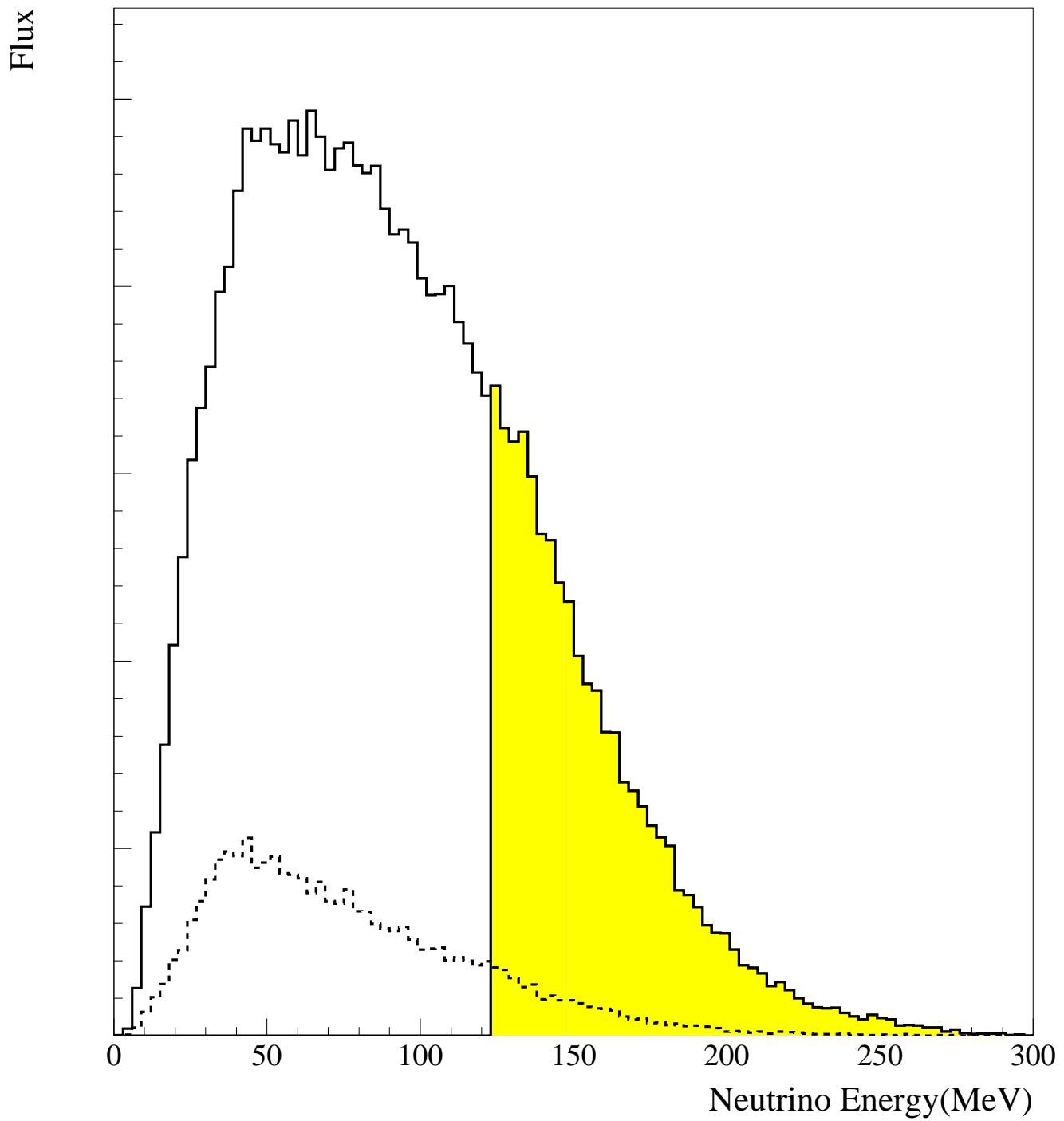


FIG. 1. The solid line shows the flux shape of  $\nu_\mu$  from  $\pi^+$  decay-in-flight. The region above muon production threshold is shaded. The dashed line shows the  $\bar{\nu}_\mu$  flux from  $\pi^-$  decay-in-flight for the same integrated proton beam.

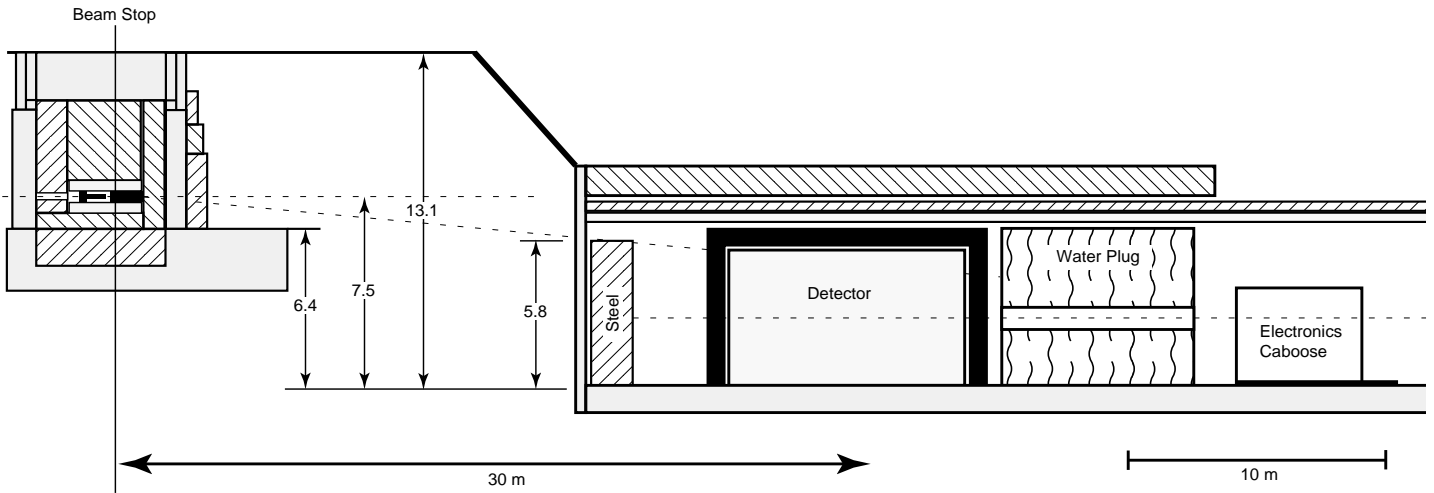


FIG. 2. The detector enclosure and target area configuration, elevation view.

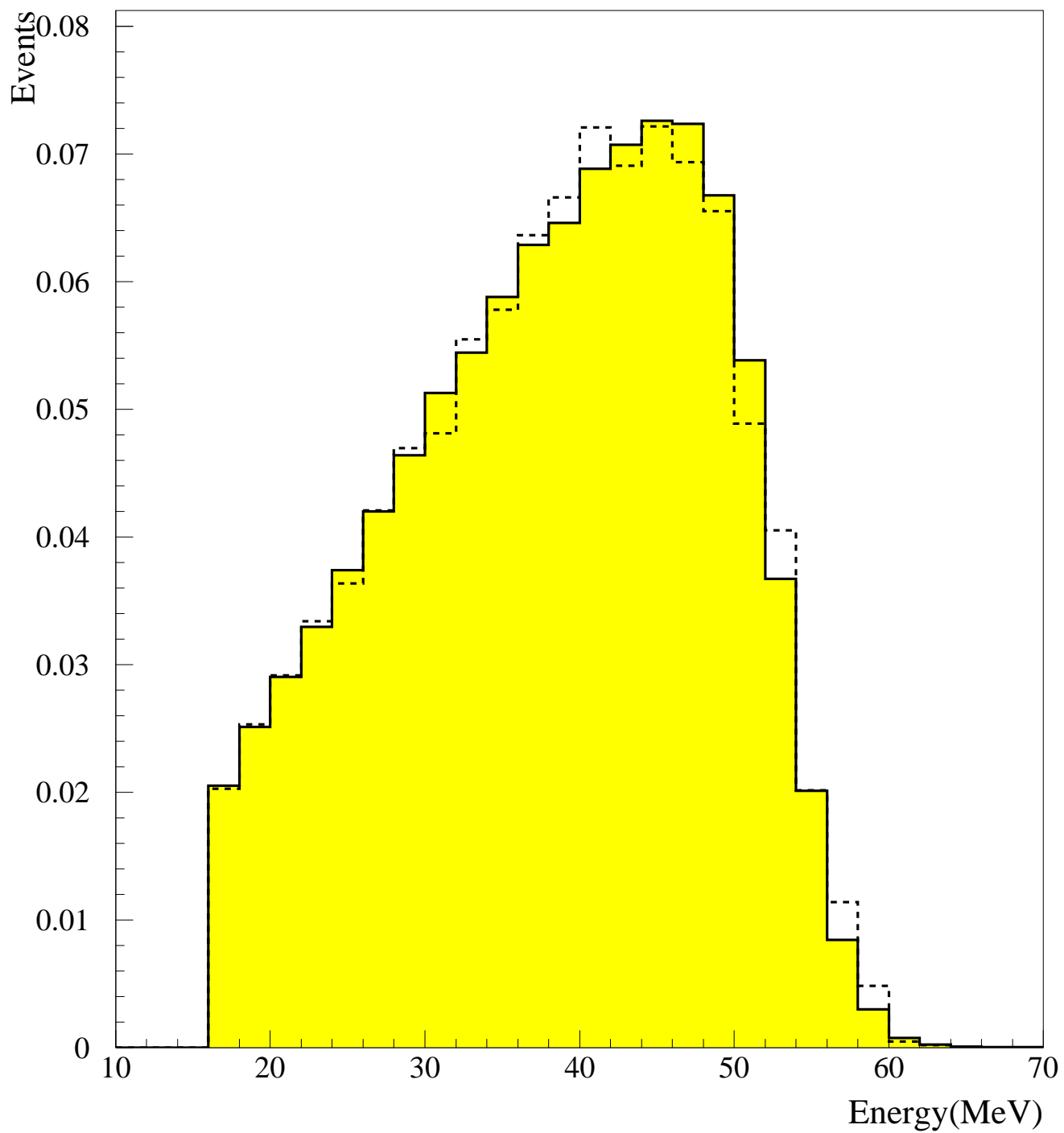


FIG. 3. The energy distribution for Michel electrons from data (solid) and simulation (dashed).

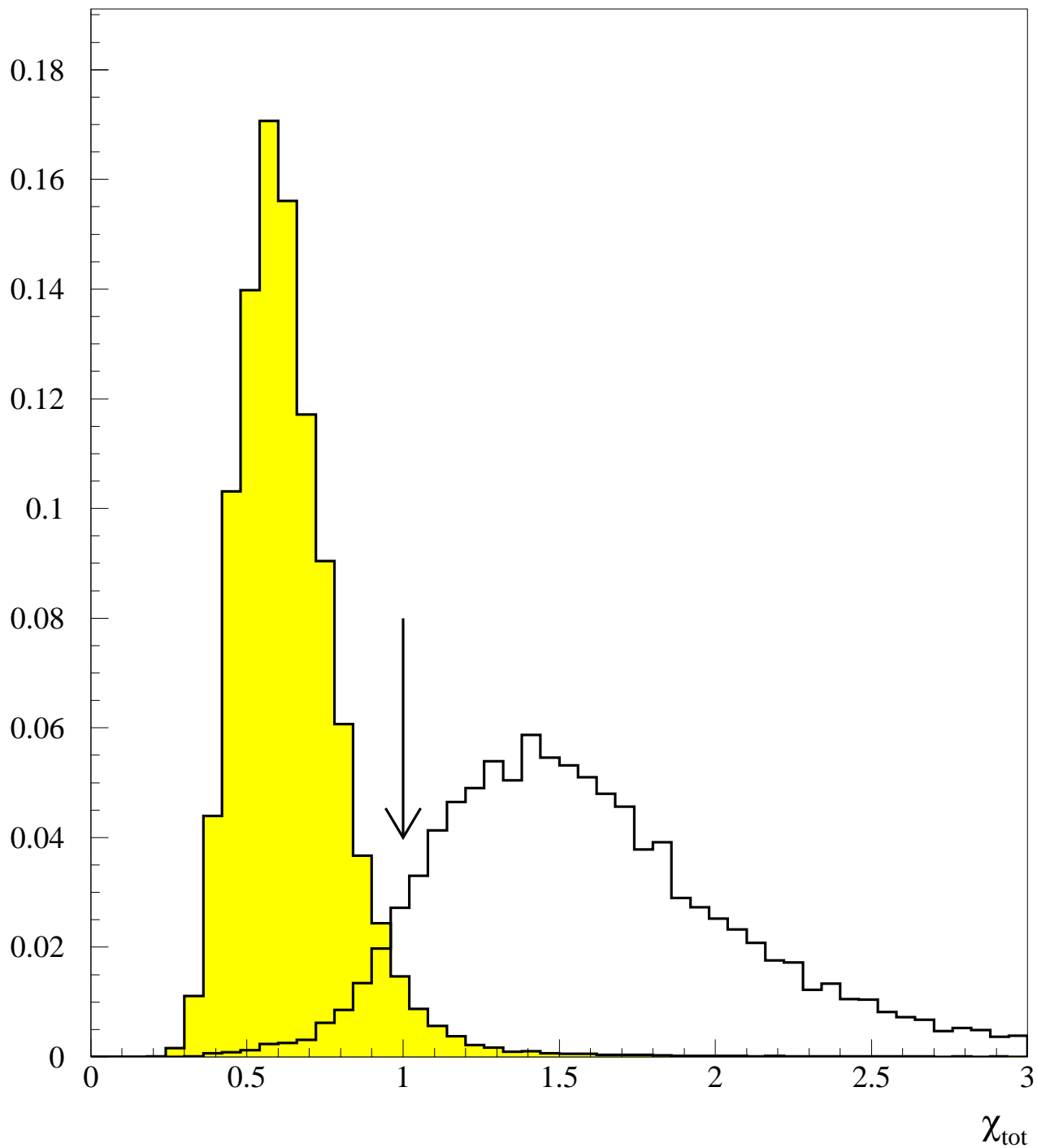


FIG. 4. Particle ID parameter for “electrons” (shaded) and “neutrons”.

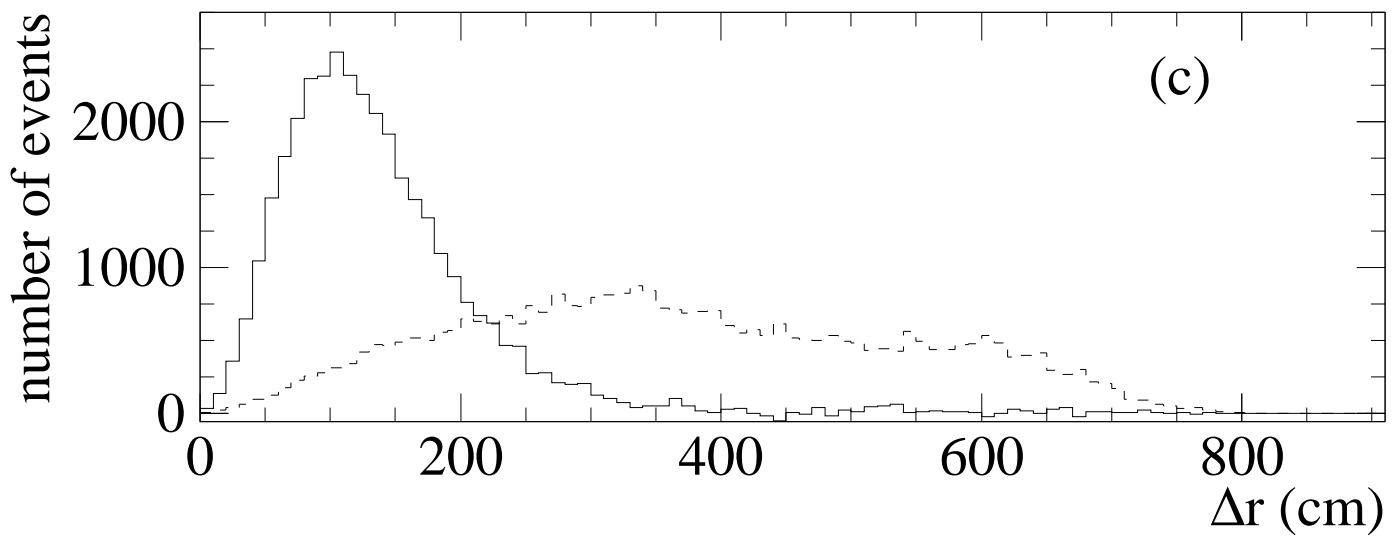
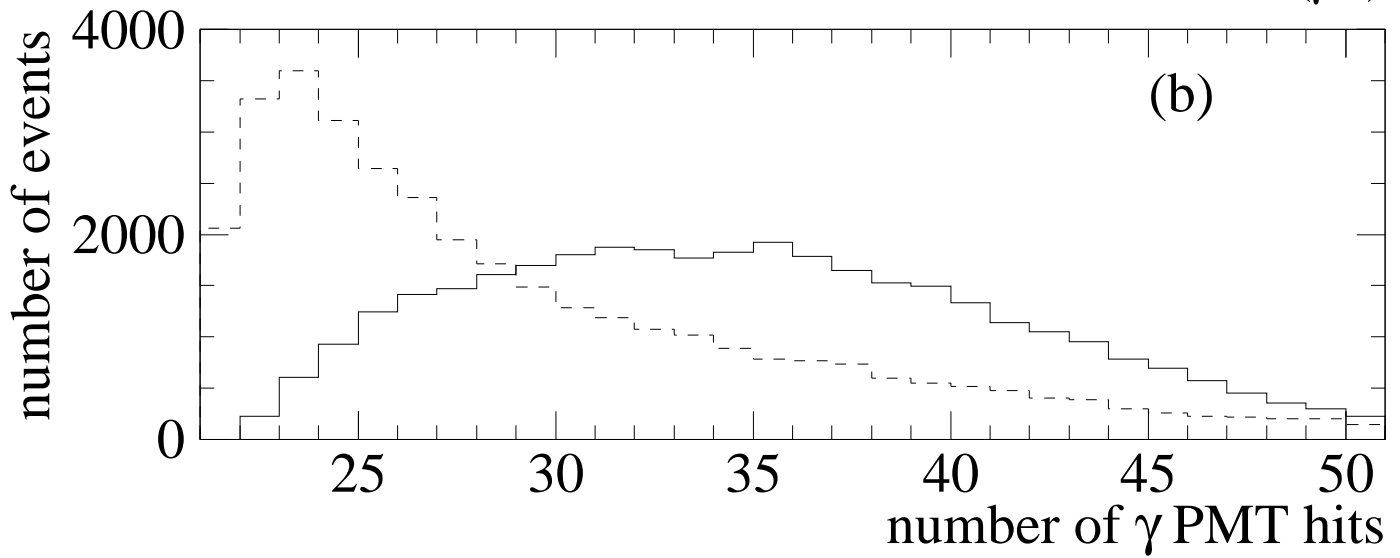
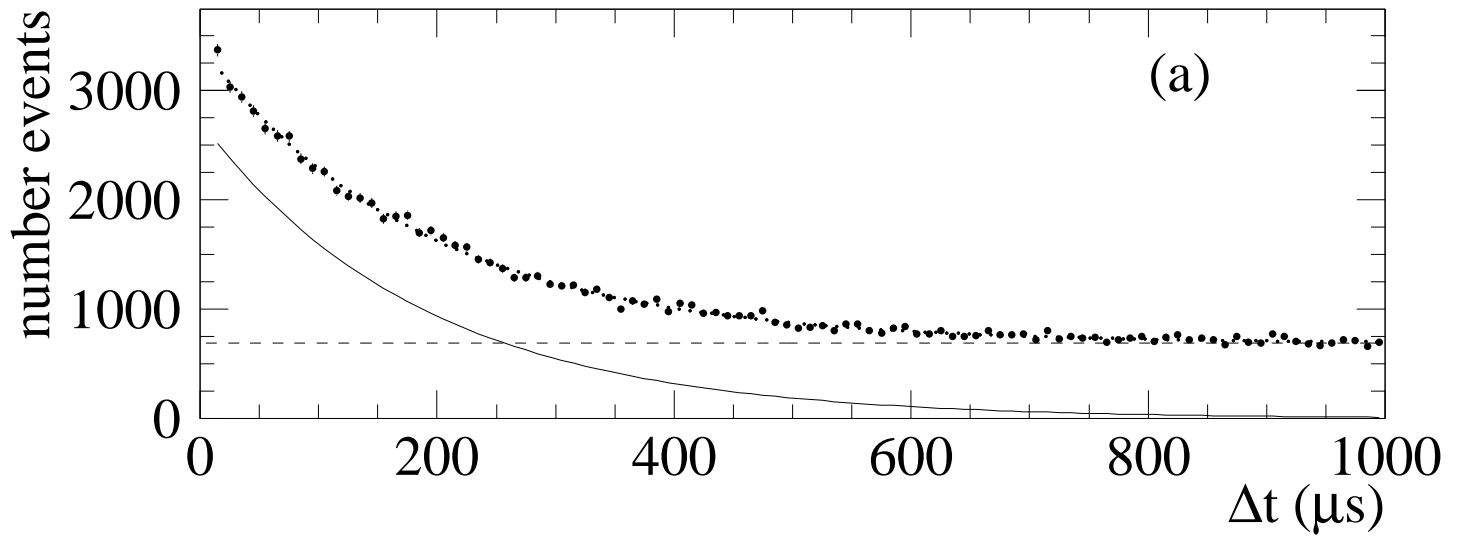


FIG. 5. Distributions obtained from cosmic-ray neutron data for  $\gamma$ 's that are correlated (solid) or uncorrelated (dashed) with the primary event: (a) the time between the photon and primary event; (b) the number of photon PMT hits; and (c) the distance between the photon and primary event. The raw data points are also shown in (a).

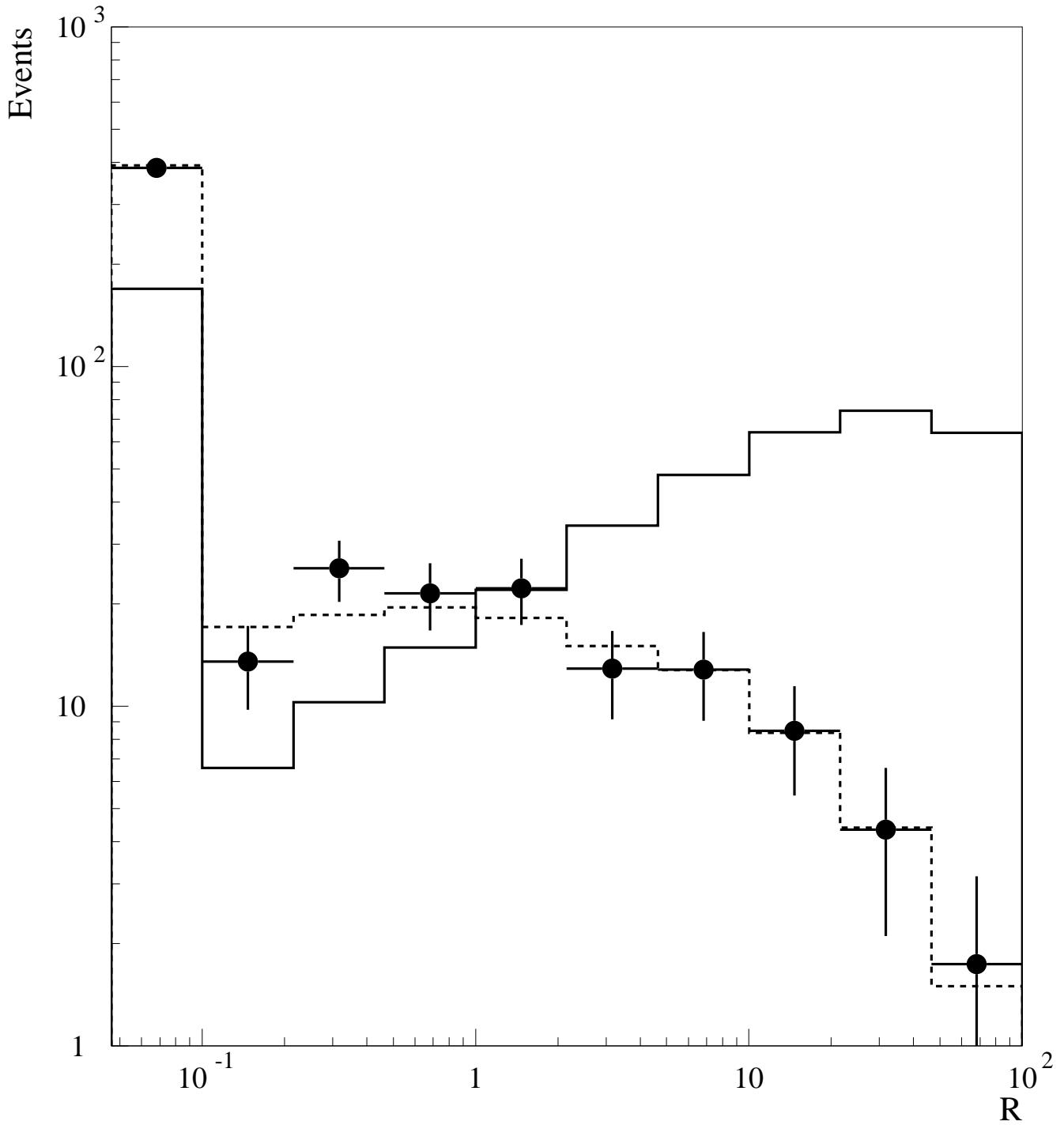


FIG. 6. The measured  $R$  distribution for events with the  $\gamma$  correlated (solid) or uncorrelated (dashed) with the primary event. Also shown is the observed  $R$  distribution for a neutrino process with no correlated  $\gamma$ 's,  $^{12}\text{C}(\nu_e, e^-)^{12}\text{N}_{g.s.}$ .

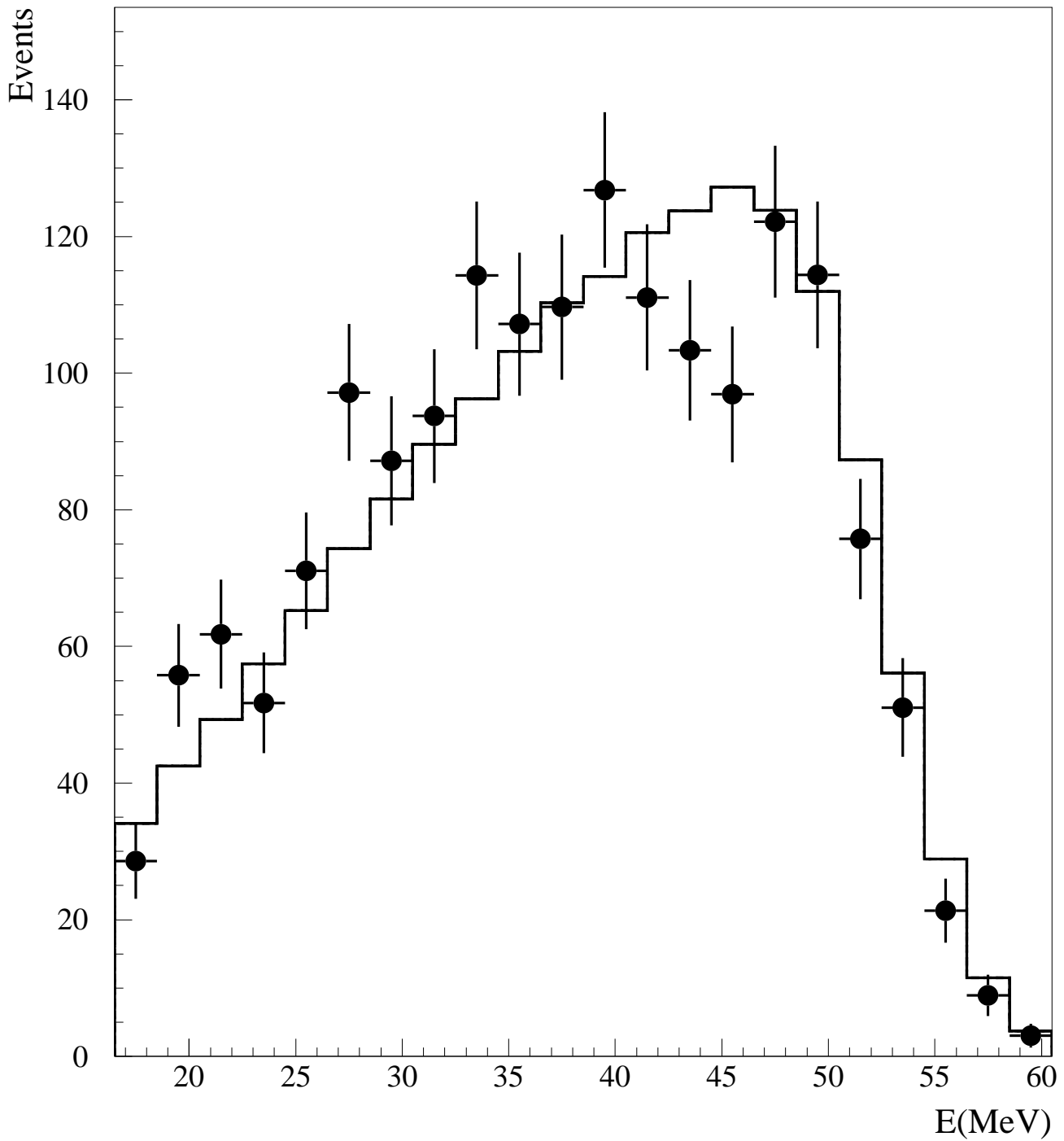


FIG. 7. The observed energy spectra of electrons from the decays of muons for the inclusive neutrino sample (points) and for the stopping cosmic ray muon sample (solid line).

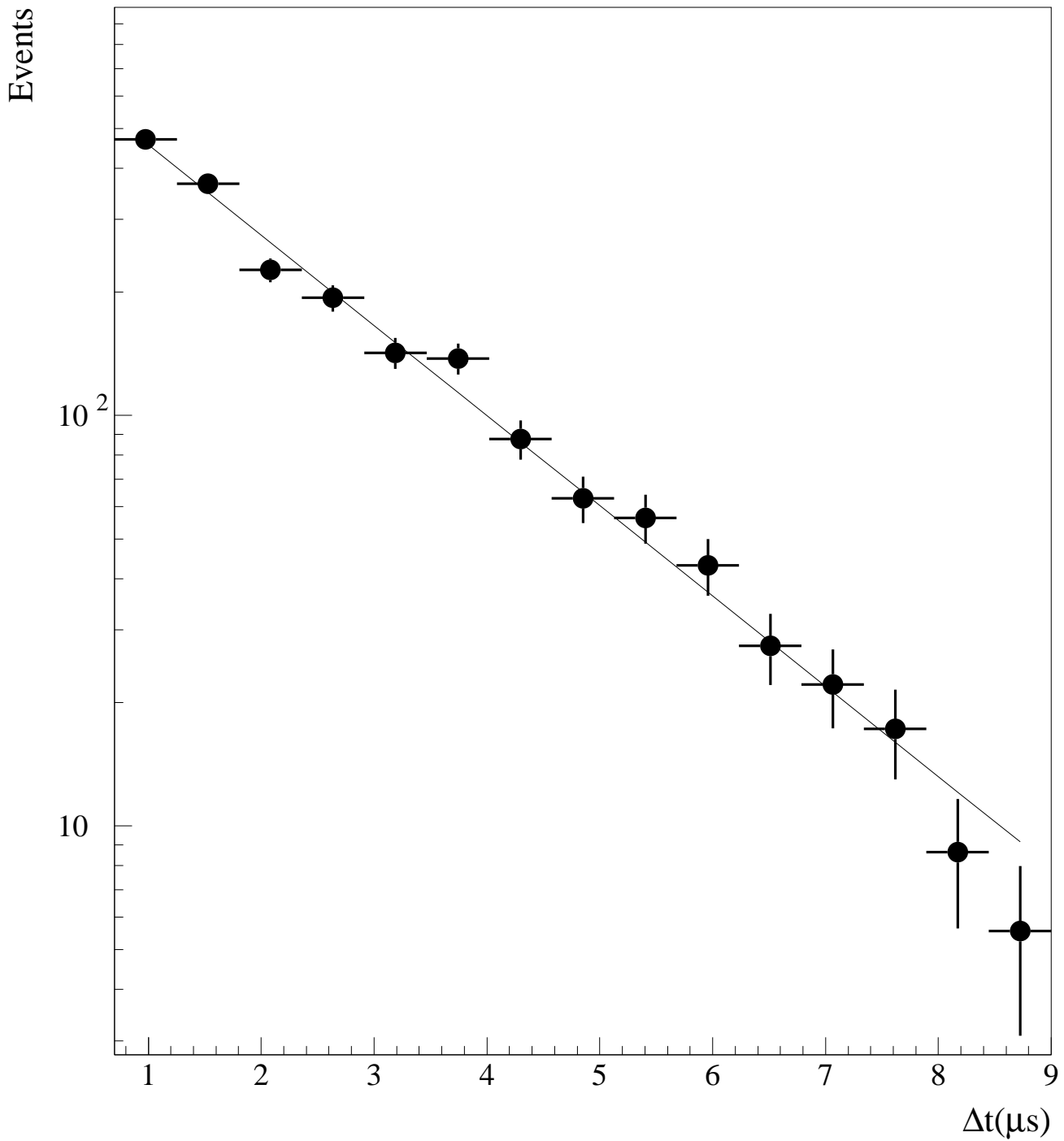


FIG. 8. The distribution of time  $\Delta t_{\mu e}$  between the  $\mu^-$  and the decay  $e^-$  in the inclusive sample,  $^{12}\text{C}(\nu_{\mu}, \mu^-)\text{X}$ . The best fit (solid line) curve corresponds to a lifetime of  $1.98 \pm 0.06 \mu s$ .

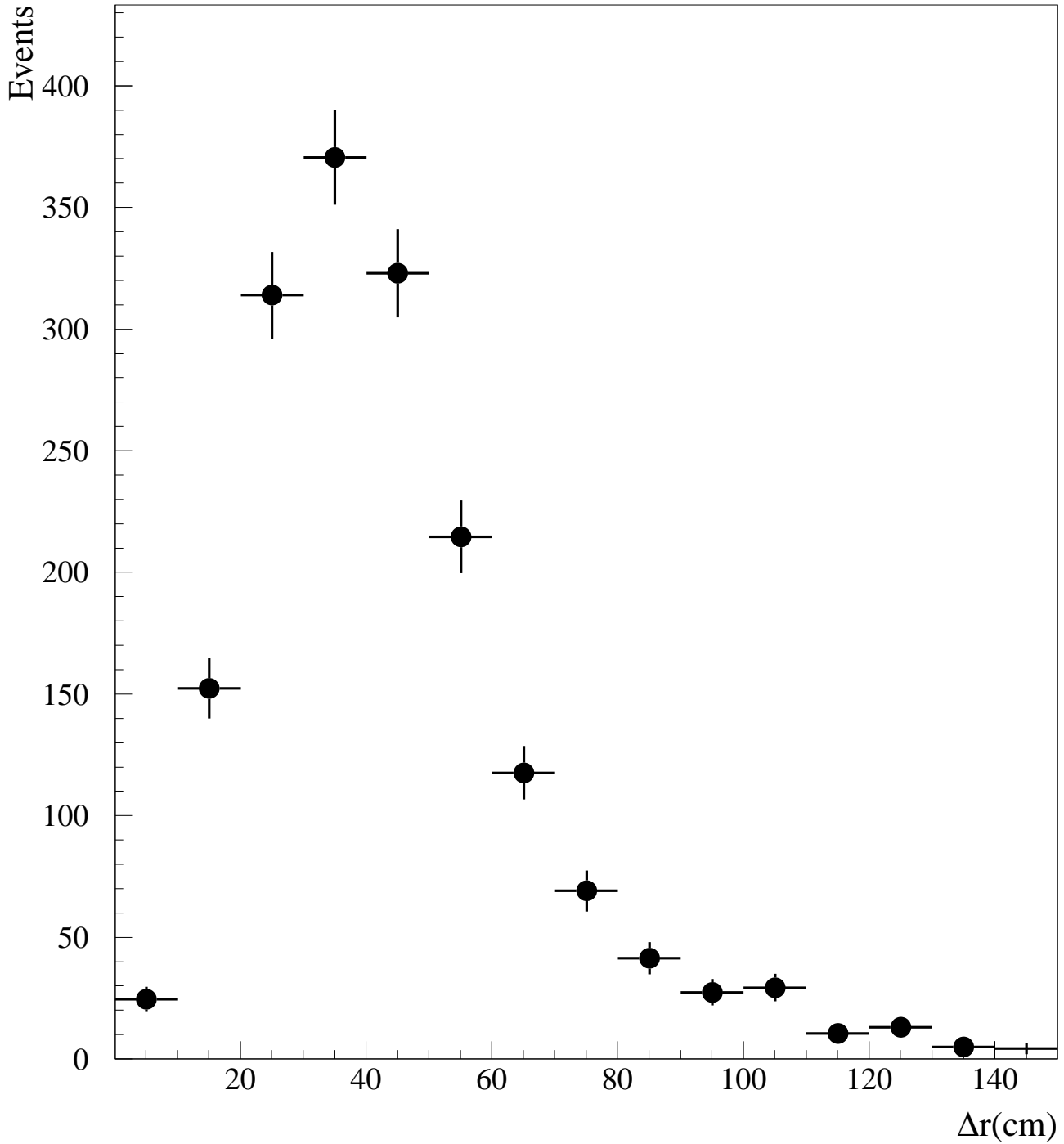


FIG. 9. The distribution of the distance between the reconstructed position of the  $\mu^-$  and the  $e^-$  in the beam-excess inclusive sample,  $^{12}\text{C}(\nu_\mu, \mu^-)\text{X}$ .

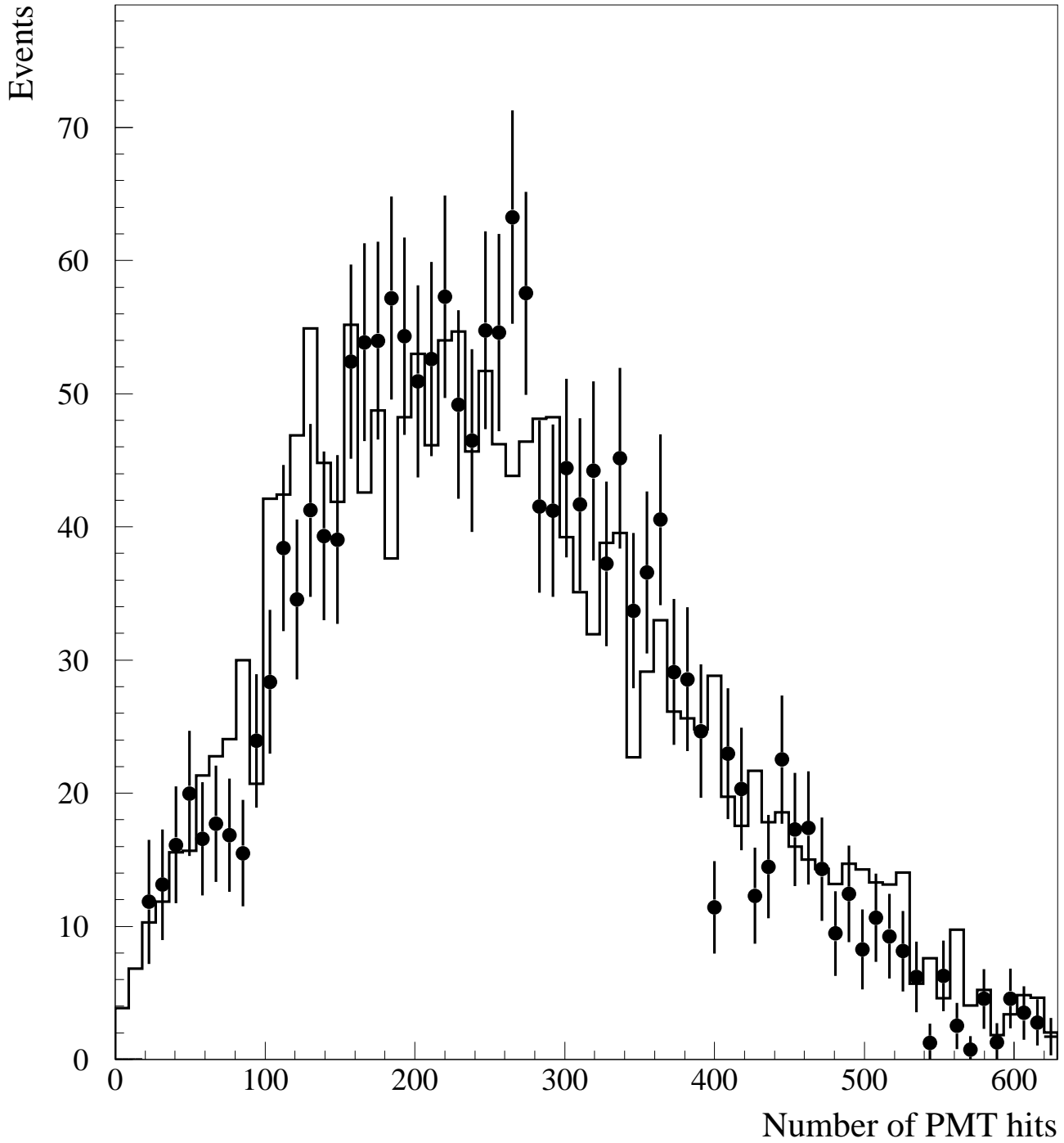


FIG. 10. The observed PMT hit distribution for the decay-in-flight sample (including  $\nu_\mu C \rightarrow \mu^- X$ ,  $\bar{\nu}_\mu C \rightarrow \mu^+ X$ , and  $\bar{\nu}_\mu p \rightarrow \mu^+ n$ ). The solid histogram is the prediction from the Monte Carlo simulation, normalized to the data.

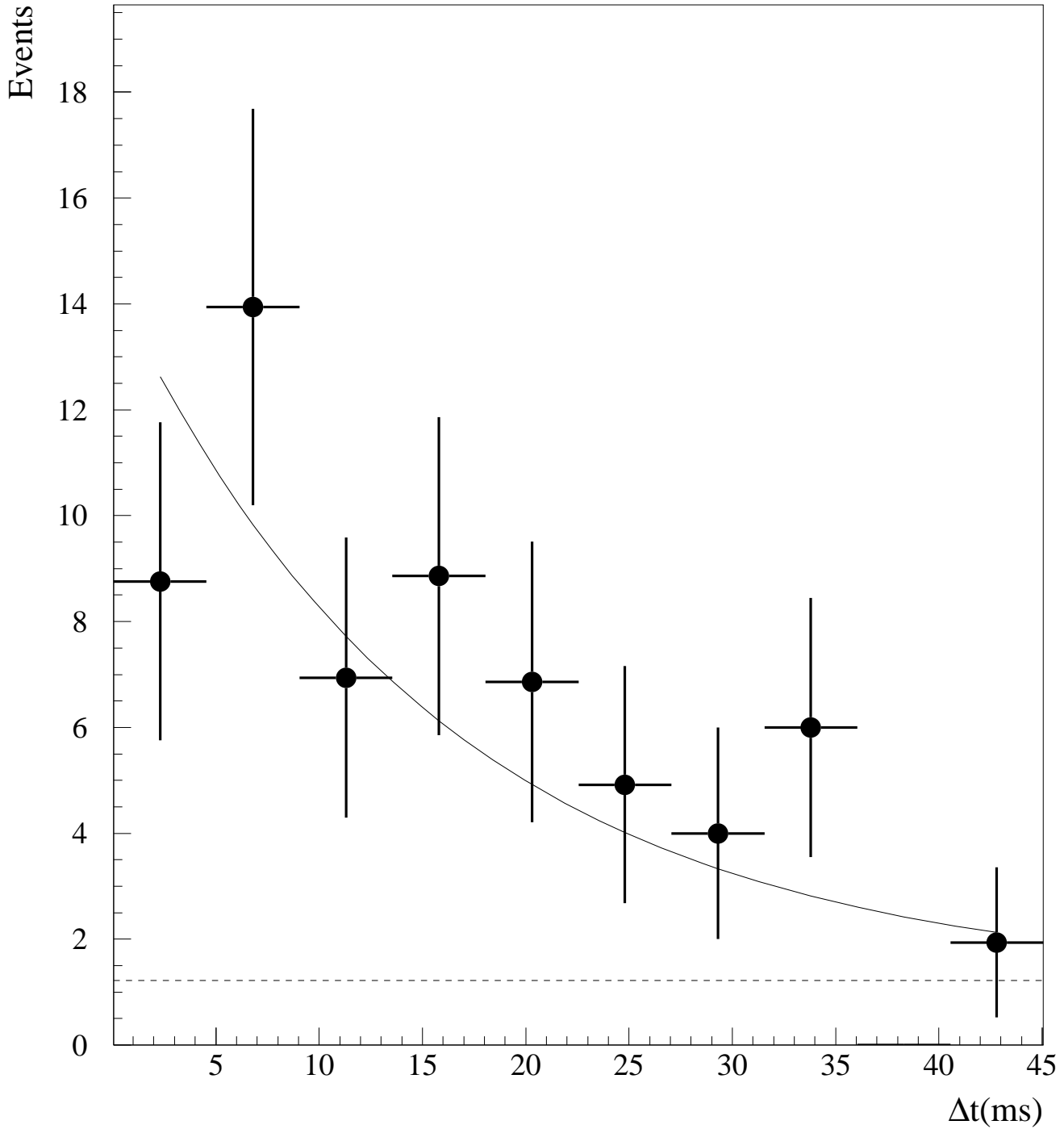


FIG. 11. The distribution of time between the  $e^-$  and  $e^+$  for beam-excess events in the  $^{12}\text{C}(\nu_{\mu}, \mu^-)^{12}\text{N}_{g.s.}$  sample. The expected distribution is shown with the solid line. The calculated accidental contribution is shown by the dashed line.

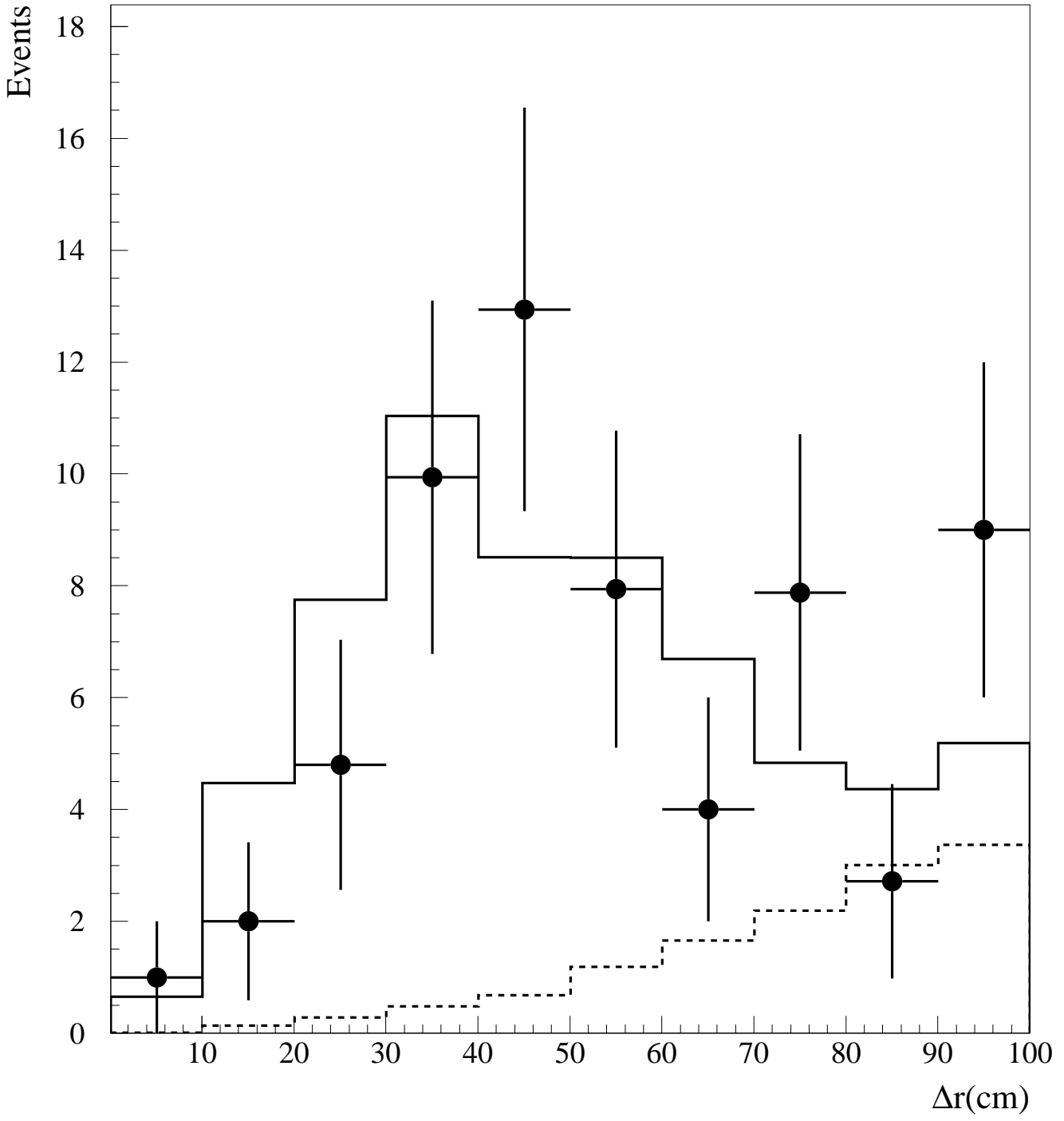


FIG. 12. The distribution of the distance between the reconstructed positions of  $e^-$  and  $e^+$  for beam-excess events in the  $^{12}\text{C}(\nu_\mu, \mu^-)^{12}\text{N}_{g.s.}$  sample. The dashed line shows the calculated accidental contribution. The solid line shows the expected shape (including the accidental contribution) obtained with a large sample of events from the reaction  $^{12}\text{C}(\nu_e, e^-)^{12}\text{N}_{g.s.}$

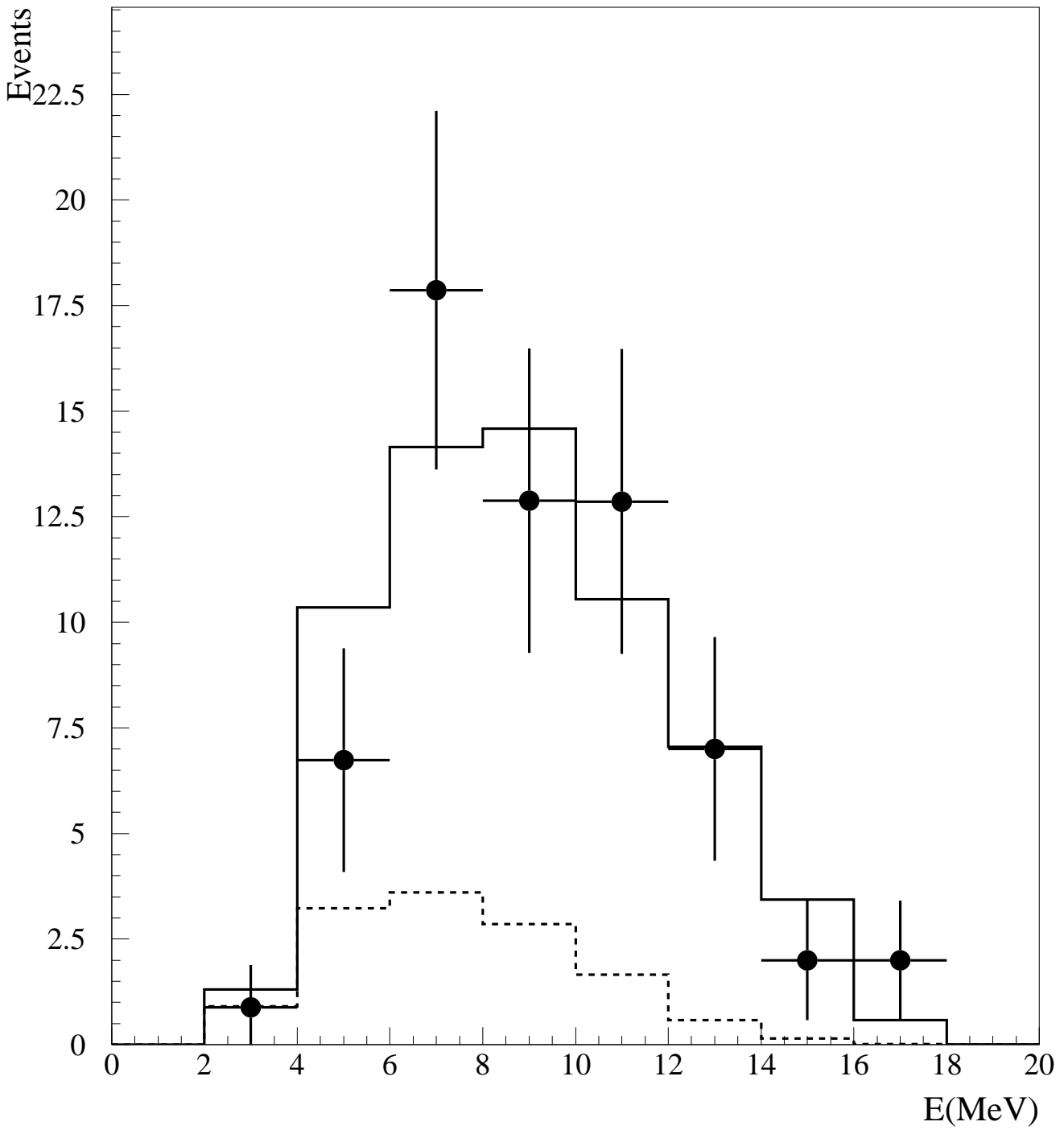


FIG. 13. The observed and expected (solid line)  $e^+$  energy distribution for beam-excess events in the  $^{12}\text{C}(\nu_{\mu},\mu^-)^{12}\text{N}_{g.s.}$  sample. The expected distribution was obtained with a large sample of events from the reaction  $^{12}\text{C}(\nu_e,e^-)^{12}\text{N}_{g.s.}$ . The dashed line shows the expected contribution from background sources.

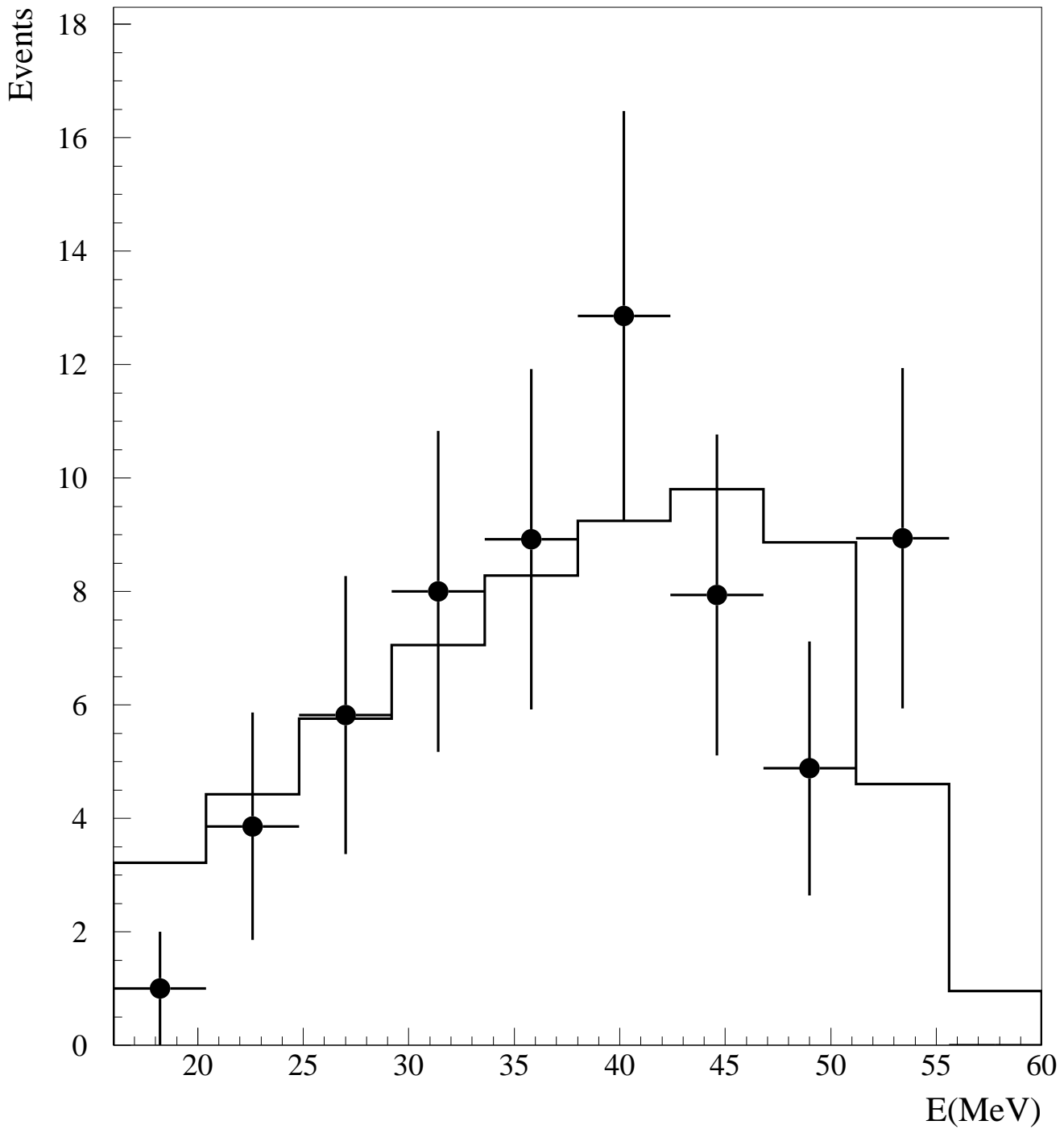


FIG. 14. The observed and expected (solid line)  $e^-$  energy distribution for beam-excess events in the  $^{12}\text{C}(\nu_\mu, \mu^-)^{12}\text{N}_{g.s.}$  sample. The expected distribution was obtained from a large sample of stopping cosmic ray events.

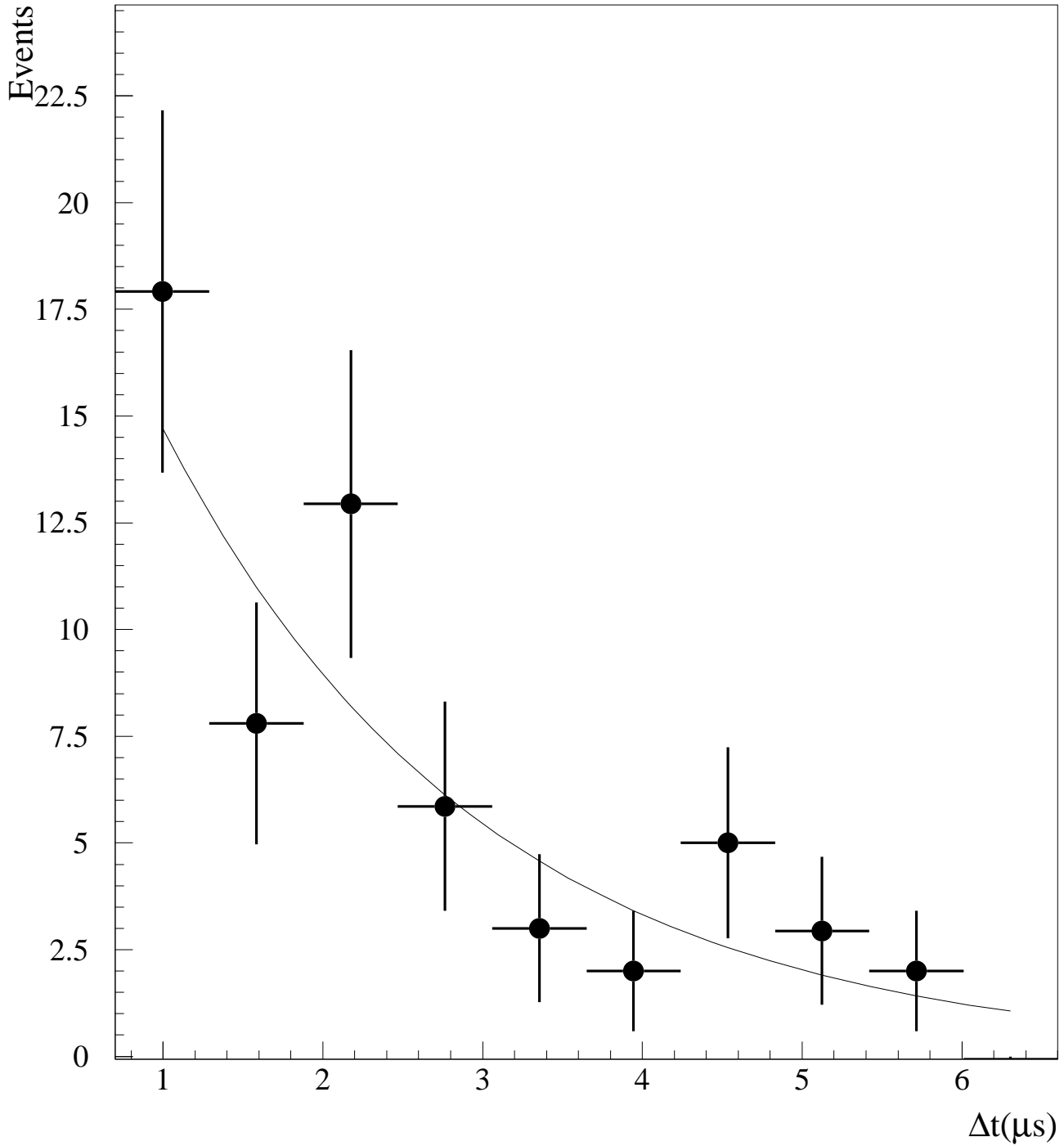


FIG. 15. The obtained and expected (solid line) distribution of time between the  $\mu^-$  and the subsequent decay  $e^-$  for beam-excess events in the  $^{12}\text{C}(\nu_{\mu}, \mu^-)^{12}\text{N}_{g.s.}$  sample.

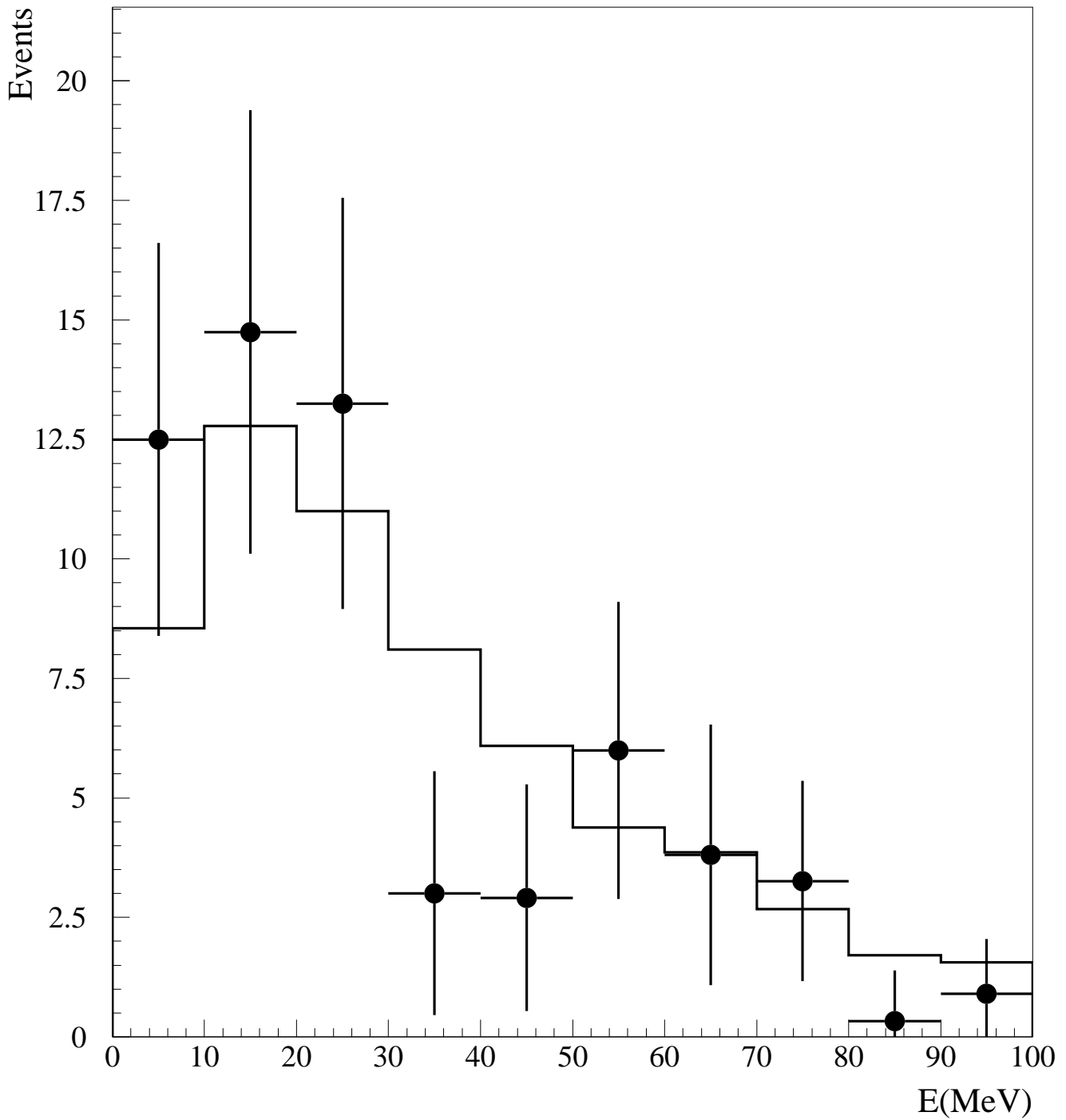


FIG. 16. The observed and expected (solid line)  $\mu^-$  kinetic energy distribution for beam excess-events in the  $^{12}\text{C}(\nu_{\mu}, \mu^-)^{12}\text{N}_{g.s.}$  sample.

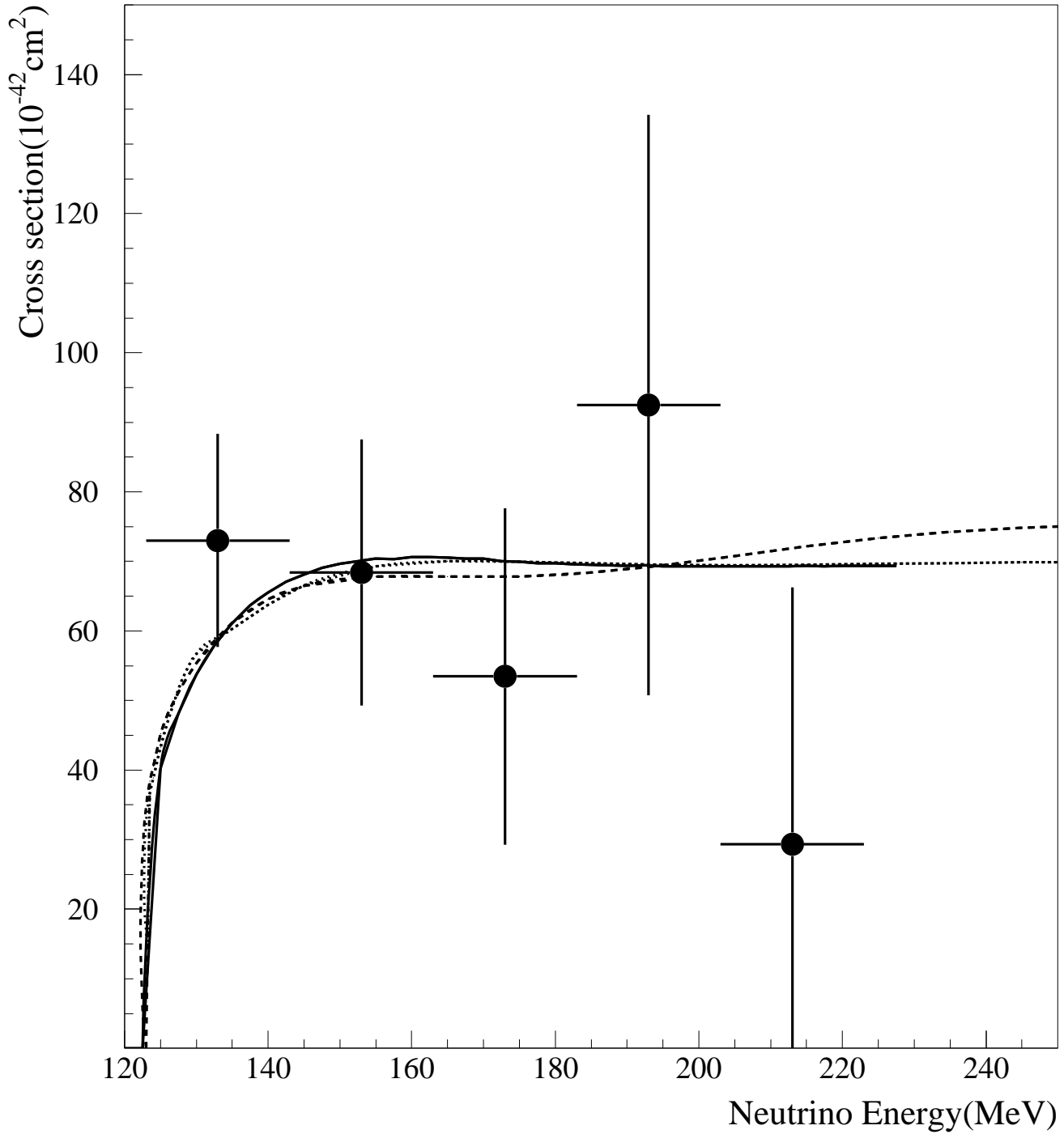


FIG. 17. The measured cross section for the process  $^{12}\text{C}(\nu_{\mu}, \mu^{-})^{12}\text{N}_{g.s.}$  compared with three theoretical calculations obtained from Ref. 20.

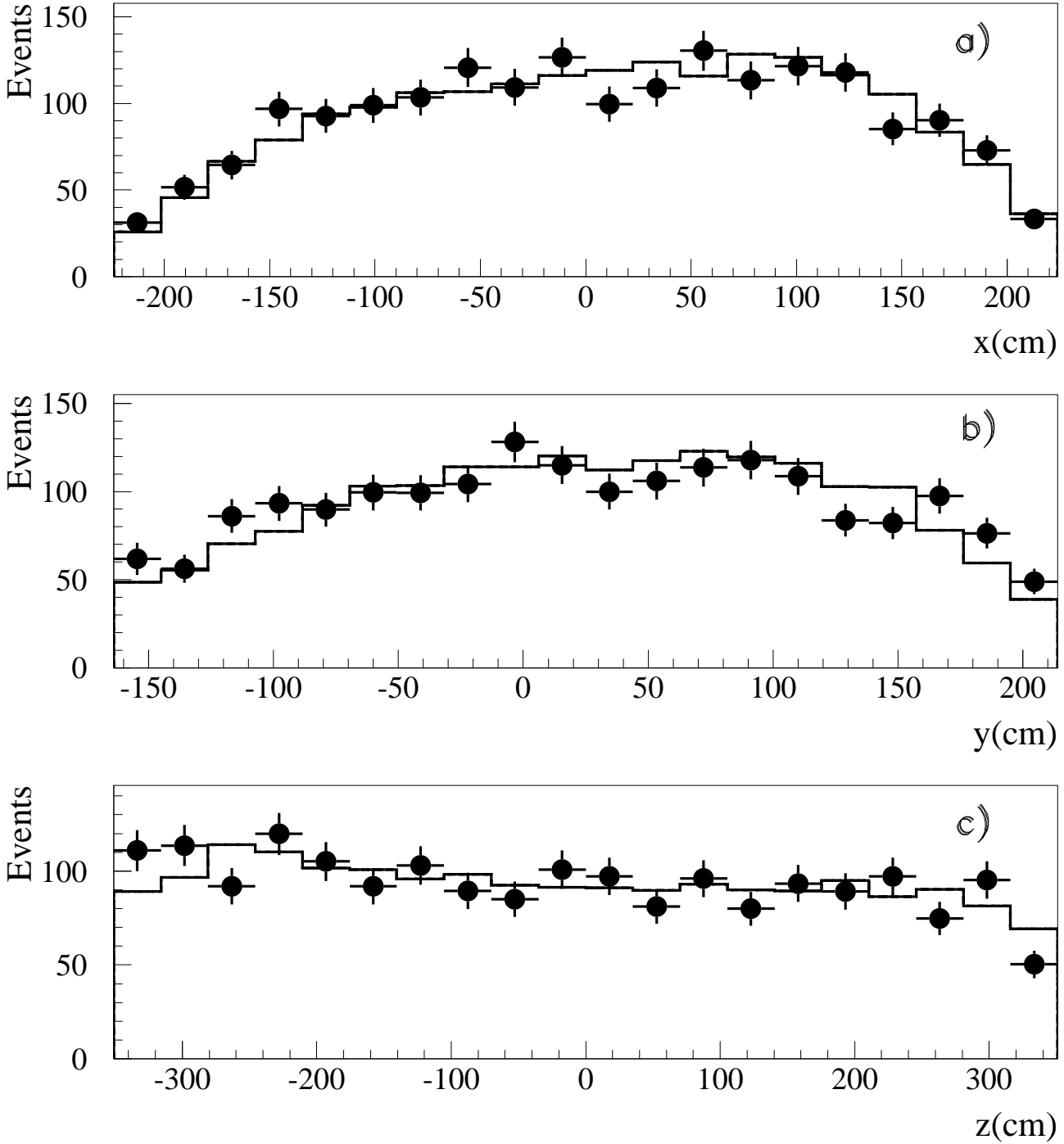


FIG. 18. The observed spatial distribution of beam-excess electrons compared with the expected (solid line) distribution for the process  $^{12}\text{C}(\nu_{\mu}, \mu^{-})^{12}\text{X}$

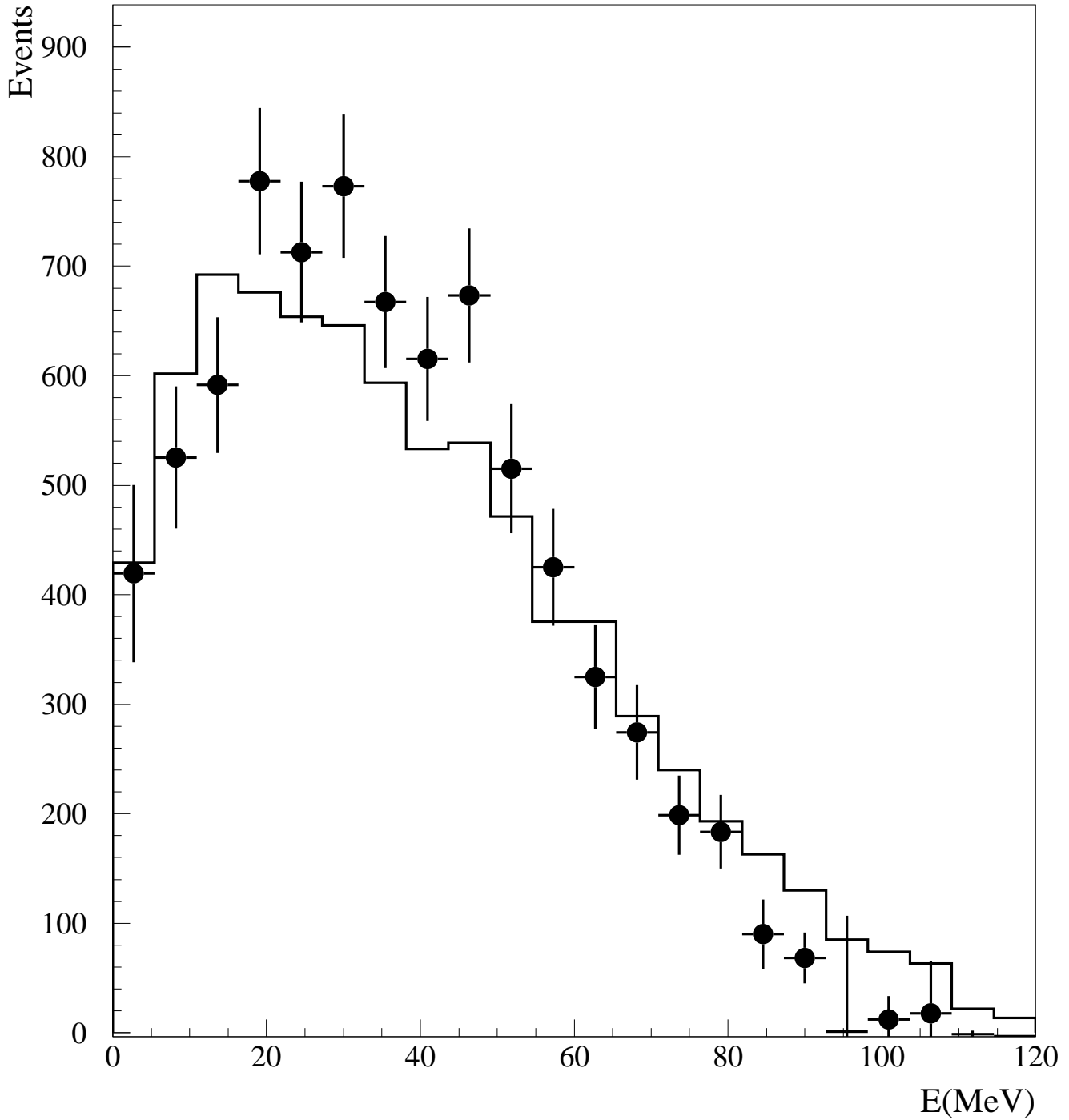


FIG. 19. The observed and expected distribution of the muon kinetic energy,  $E_\mu$ , for the inclusive decay-in-flight sample. The expected distribution has been normalized to the data.

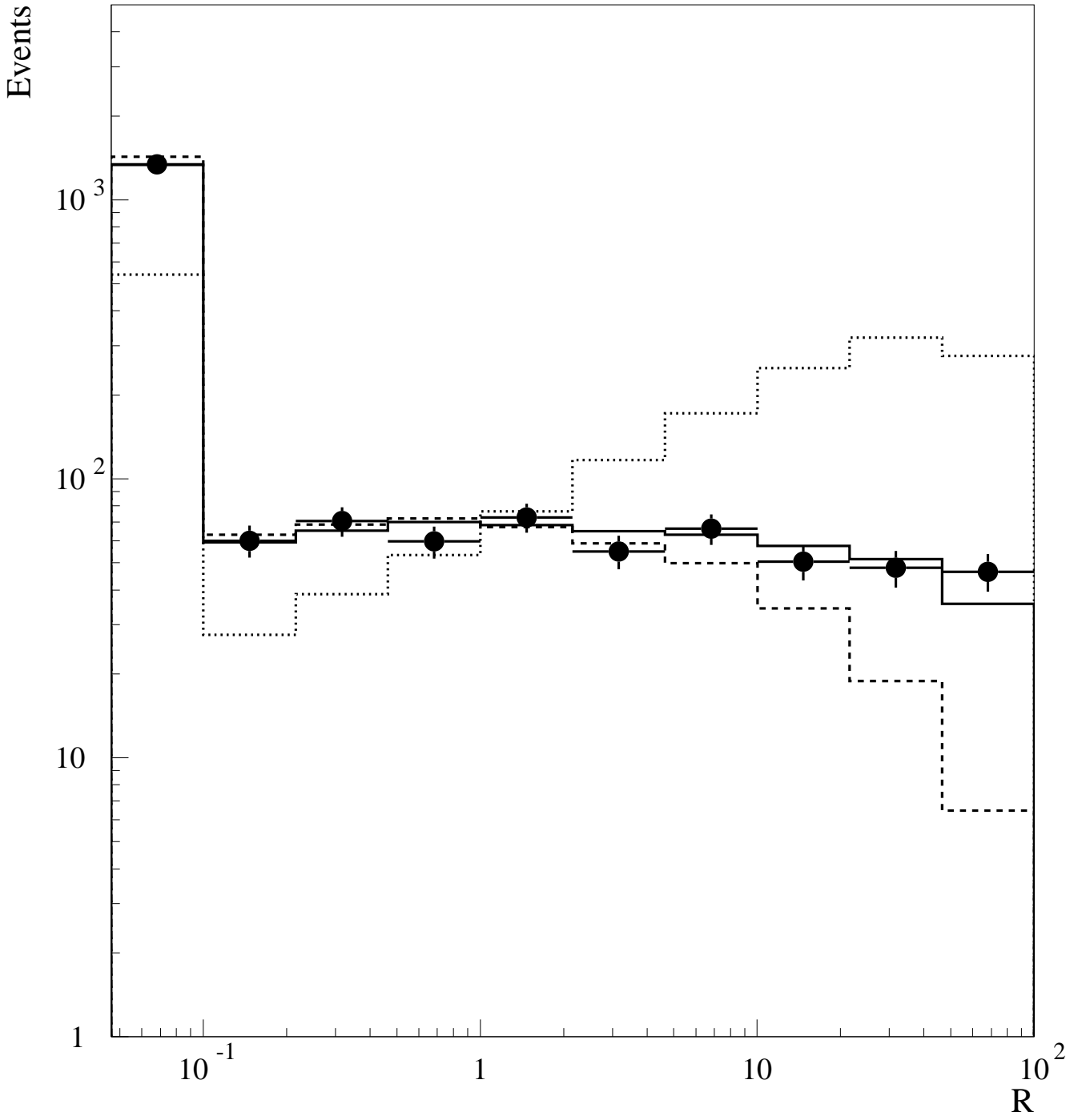


FIG. 20. The observed distribution of the  $\gamma$  likelihood ratio  $R$  for the inclusive decay-in-flight sample. Shown for comparison are the correlated distribution (dotted line), the uncorrelated distribution (dashed line) and the best fit (solid line) to the data which has a  $(10.8 \pm 1.8)\%$  correlated component.

## REFERENCES

1. D.A. Krakauer *et al.*, Phys. Rev. C **45**, 2450 (1992).
2. B.E. Bodmann *et al.*, Phys. Lett. B **332**, 251 (1994).
3. C. Athanassopoulos *et al.*, Phys. Rev. C **55**, 2078 (1997).
4. M. Fukugita *et al.*, Phys. Lett. B **212**, 139 (1988).
5. E. Kolbe, K. Langanke and S. Krewald, Phys. Rev. C **49**, 1122 (1994).
6. M. Albert *et al.*, Phys. Rev. C **51**, 1065 (1995).
7. H.J. Kim *et al.* Proceedings of the 14th International Conference on Particles and Nuclei (PANIC 96), 583 (1996).
8. E. Kolbe *et al.*, Phys. Rev. C **52**, 3437 (1995).
9. A. C. Hayes, paper presented at the Joint APS/AAPT meeting, April, 18-21, 1997
10. D.D. Koetke *et al.*, Phys. Rev. C **46**, 2554 (1992).
11. C. Athanassopoulos *et al.*, Phys. Rev. C **54**, 2685 (1996).
12. C. Athanassopoulos *et al.*, submitted to Nucl. Instrum. Methods.
13. S. Willis *et al.*, Phys. Rev. Lett. **44**, 522 (1980).
14. S.J. Freedman *et al.*, Phys. Rev. D **47**, 811 (1993).
15. R.C. Allen, *et al.*, Nucl. Instrum. Methods A **284**, 347 (1989).

16. R.L. Burman, M.E. Potter and E.S. Smith, Nucl. Instrum. Methods A **291**, 621 (1990).
17. R.A. Reeder *et al.*, Nucl. Instrum. Methods A **334**, 353 (1993).
18. J. Napolitano, *et al.*, Nucl. Instrum. Methods A **274**, 152 (1989).
19. K. McIlhany, *et al.*, Proceedings of the Conference on Computing in High Energy Physics, April 1994, LBL Report 35822, 357 (1995).
20. J. Engel, E. Kolbe, K. Langanke and P. Vogel, Phys. Rev. C **54**, 2740 (1996).
21. R. Becker-Szendy *et al.* (IMB Collaboration), Phys. Rev. D **46**, 3270 (1992).
22. K. S. Hirata *et al.* (Kamiokande Collaboration), Phys. Lett. B **280** 146 (1992).